Density dependence of excess electronic ground-state energies in simple atomic fluids

B. Space[a] and D. F. Coker[b]
Department of Chemistry, Boston University, 590 Commonwealth Avenue, Boston, Massachusetts 02215

Z. H. Liu[c] and B. J. Berne
Department of Chemistry, Columbia University, New York, New York 10027

G. Martyna
Department of Chemistry, University of Pennsylvania, Philadelphia, Pennsylvania 19104-6323

(Received 22 January 1992; accepted 23 April 1992)

The ground-state energies of an excess electron E_0 as a function of solvent density are computed using model electron–atom pseudopotentials in fluid helium, argon, and xenon. E_0 is a lower bound to the experimentally measurable threshold to photoconductivity, V_0. The nonuniqueness of the pseudopotential description of electron–molecule interactions is demonstrated. We find that when many-body polarization effects are included, our calculated E_0 results are in close agreement with experimental V_0 values indicating that the conduction-band energy lies close to the ground-state energy across a broad range of densities in these polarizable fluids. If the many-body nature of the polarization interaction is ignored the ground-state energies deviate significantly from the V_0 results highlighting the importance of accurate treatment of many-body polarization interactions. It is shown that a mean-field theory of polarization gives substantial agreement with full many-body calculations. This allows us to introduce a mean-field, density-dependent pair potential which greatly simplifies such many-body calculations. In the more polarizable systems, it is found that the spatial extent of the ground-state wave function as a function of solvent density is correlated with the density dependence of both V_0 and the electron mobility, and it becomes uniformly spread throughout our simulation cell as the electron mobility goes through its maximum value at intermediate solvent densities.

I. INTRODUCTION

In this paper we explore the density dependence of the excess electronic ground-state energy in a number of simple fluids including helium, argon, and xenon. The experimental observable is quite a different quantity. To probe the energetics of the electrons in fluids the difference between the work function of a metal electrode immersed in the solvent, and the work function of the metal electrode in vacuum, is measured.[1,2] This quantity, called V_0, is the threshold above which conduction can occur and can thus be interpreted as is a measure of the lowest-energy conducting state. In some systems, the lowest-energy states may be strongly localized, leading to trapping of the electron in density fluctuations of the host fluid, with corresponding energy eigenvalues lower than the bottom of the conduction band, V_0. Alternatively, the topology of the electron–solvent potential surface can be such that the lowest-energy states are spatially delocalized and coupled by thermal motions of the solvent. Under these circumstances, the ground state will be the bottom of the conduction band. Thus, the ground-state energy is a lower bound on V_0.

The precise connection between the experimentally observed V_0 values and our calculated E_0 results is nontrivial. The only thing we can be certain about is that the density-dependent V_0 curve must lie entirely above the E_0 curve. If E_0 shows a minimum and upturn as a function of density then V_0 must either lie on top of E_0 or above it, in which case the V_0 curve may have a sharper minimum and upturn, and the minima of the two curves need not necessarily correspond to the same density. Interestingly, we find that both in argon and xenon, when many-body polarization effects are included, the density at which our calculated E_0 values have their minimum corresponds almost exactly to the density at which the experimental V_0 values have their minimum. If many-body polarization effects are ignored our calculated E_0 results have their minimum at more than twice this density. In argon we find that the experimental V_0 and calculated E_0 results lie almost on top of one another, where as in xenon the experimental V_0 values have a sharper upturn with density than the calculated E_0 results. This finding is consistent with the idea that the lowest-energy conducting state in argon is very close in energy to the ground state across the entire range of fluid densities. In xenon, however, the lowest-energy conducting states at low and high densities probably lie somewhat above the ground state whereas around the minimum the first conducting state may be close in energy to the ground state.

In a simple nonpolarizable hard-sphere fluid, such as helium, the value of V_0 is found to increase monotonically

[a] In partial fulfillment of the Ph.D. in Chemistry from Boston University.
[b] Presidential Young Investigator.
[c] In partial fulfillment of the Ph.D. in Chemical Physics from Columbia University.

 0021-9606/92/152002-20$006.00

with increasing density. In fluids of polarizable atoms such as argon or xenon, on the other hand, the value of V_0 first decreases with increasing density, reaching a minimum in the dense liquid. The value of V_0 then increases with increasing density beyond this minimum point. The *reduced* density at which the V_0 minimum occurs shows a solvent dependence, the more polarizable and larger the solvent atoms, the higher the *reduced* density at which the V_0 minimum occurs.

Dynamical properties, like the electron mobility, show related trends with density. In nonpolarizable solvents, the mobility simply decreases monotonically with increasing density. In fluids of highly polarizable atoms, on the other hand, the mobility decreases steadily through the gaseous density regime, reaching a minimum around the critical density. In the liquid region the mobility increases dramatically, reaching its peak value at almost exactly the same density as the minimum in V_0. Further increases in density beyond this point result in a rapid decrease in mobility, followed by a slight upturn as the solid is approached. Interestingly, the maximum mobility in argon is about 10 times that of electrons in metallic copper, while in the more polarizable xenon, electrons are about 50 times more mobile than in copper!

In earlier work, Coker, Thirumalai, and Berne[3] used path-integral methods to explore the equilibrium properties of excess electrons in various simple fluids. Sprik, Klein, and Chandler[4,5] used similar methods to study the properties of hard-sphere models of these systems and showed that an approximate analytic theory (RISM polaron theory) could give accurate results. Laria and Chandler[6] showed that these hard-sphere analytic models could be fit to give reliable agreement with simulations using more accurate pseudopotentials. Coker and Berne[7] explored the onset of photoconducting states of electrons equilibrated in fluid helium and tested a simple Wigner–Seitz–like model.[8] This simple model theory has been used by Plenkiewicz, Plenkiewicz, and Jay-Gerin[9–11] to study the density dependence of conducting-state energies of electrons injected into unperturbed fluids. Recently, Stampfli and Bennemann[12] presented a new type of Wigner–Seitz model which takes account of the fluid disorder in terms of fractional filling of a crystal lattice. They use a simple model potential incorporating a fitted hard-core repulsion at short range, pair polarization within the Wigner–Seitz cell, and a dielectric continuum approximation for the long-range many-body polarization contribution and obtain results in good agreement with experiment.

The electronic properties of fluids of polarizable atoms are determined by the balance of short-range repulsive and long-range attractive electron–solvent interactions. The most important attractive interaction between the electron and the solvent atoms is induction or polarization. This arises when a point charge induces a dipole in a polarizable atom. When the system consists of many polarizable atoms the dipoles will interact with themselves as well as with the point charge. Simulation calculations by Wallqvist, Martyna, and Berne,[13] using the full solution of the self-consistent induced-dipole equations to study an excess electron in water, showed that many-body effects accounted for about 10% of the total excess electronic energy. Martyna and Berne[14,15] used these methods to explore the importance of induced many-body interactions for electron attachment to clusters of xenon atoms and found that using an accurate many-body interaction could give energies as much as a factor of 2 higher than those obtained when induced-dipole–induced-dipole interactions are neglected, i.e., a pair polarization potential is used.

A convenient mean-field approach to this many-body polarization problem for electrons in liquids was presented by Lekner.[16] This approach is used in ground-state calculations on electrons in clusters by Martyna and Berne and in path-integral calculations on electrons in fluid xenon by Coker and Berne.[17] The latter found that the density dependence of the average electronic energy showed the same qualitative trends as experimental V_0 values when many-body effects were included but showed substantial disagreement when a pair potential description was incorporated. Mean-field many-body polarization effects were also included in the Wigner–Seitz model calculations of Plenkiewicz and co-workers and in recent path-integral molecular-dynamics (MD) studies of the mean energies for electrons in argon.[18] Dielectric continuum theories[19,12,20] provide a simple approximate way to include many-body polarization effects and have been used successfully to describe both clusters and bulk phase systems of nonpolar molecules.

Recently, a number of analytic theories of excess electrons in polarizable fluids have been developed based on pair potential descriptions of the electron–solvent interactions. Of note here are the RISM–polaron theory calculations of electron mobility presented by Hsu and Chandler[21] and the percolation theory model for conduction-band energies of Stratt and co-workers.[22] We show that these theories, which ignore the many-body nature of the interactions, can at best give only a qualitative description of the density dependence of electronic properties in polarizable fluids. For example, we find that if a bare pair potential is employed, the density dependence of the ground-state energy has a minimum at much higher densities (well into the compressed solid regime) than the experimental V_0 minima. When many-body effects are included, however, the position of the minimum is close to that observed with the experimental V_0 values. We believe the important nature of the potential surface is hidden in unphysical parametrizations of these approximate theories.

In this paper we also explore the nature of the excess electronic states supported by these simple fluids. The ground-state properties of static fluid configurations are obtained with both the diffusion Monte Carlo (DMC) and a block Lanczos diagonalization (BLD) method. We explore the sensitivity of various excess electronic properties to the details of the electron–molecule pseudopotential and demonstrate that the importance of the many-body polarization interaction goes beyond energetic concerns. We also demonstrate that the Lekner mean-field theory provides a very convenient and accurate way to describe this

interaction in situations where the solvent is unperturbed by the presence of the electron.

The paper is organized in three sections. In Sec. II we briefly describe the diffusion Monte Carlo and block Lanczos diagonalization methods we employ to compute the eigenstates of various representative fluid configurations. Section III details the various pseudopotentials we have considered as models of the electron–molecule interactions. Results of our electronic ground-state energy calculations for different model potentials are presented in Sec. IV where we also explore the density dependence of the eigenstates. Various conclusions based on our studies are discussed in Sec. V.

II. METHODS

To check accuracy and consistency of our results two different methods, diffusion Monte Carlo (DMC) and a fast Fourier transform (FFT) block Lanczos diagonalization (BLD) algorithm, were used to compute the adiabatic excess electronic ground states of static solvent configurations at various solvent densities. In this section, we outline the two methods and discuss their relative merits for this particular application.

The FFT BLD algorithm calculates instantaneous adiabatic electronic eigenvalues and eigenfunctions by using an efficient scheme developed by Webster, Rossky, and Friesner[23] based on an iterative Lanzcos algorithm.[24] The eigenfunctions are represented on a discrete grid of N points in space. With this representation, H is an $N\times N$ matrix whose low-energy eigenstates are to be determined. The eigenstates of $\exp(-\tau H)$ are the same as those of H but by choosing a large enough value for τ the iterative Lanczos algorithm converges more rapidly for the exponential operator than it does for H itself. Webster's algorithm involves first using the single-vector Lanczos algorithm to obtain a set of low-energy eigenstates for a short-time approximation to $\exp(-\tau H)$, namely

$$\exp(-\tau H)\sim\exp(-\tau T/2)\exp(-\tau V)\times\exp(-\tau T/2)+\mathcal{O}(\tau^3),$$

where T and V are the kinetic and potential operators. Standard fast Fourier transform methods[25] are used to compute the action of this short-time form on an arbitrary function so that the Lanczos recursion can be implemented. The set of eigenfunctions of the short-time approximation to $\exp(-\tau H)$ are now used as a starting set of basis functions for a "block Lanczos" refinement of the eigenstates of H itself with no errors due to the short-time approximation. Each block of new basis functions is generated by computing the action of H on the previous block and orthogonalizing the new functions with respect to all previous blocks as well as orthogonalizing within the current block. A block tridiagonal form of the Hamiltonian in this basis set is then computed and diagonalized using standard methods giving many accurate eigenstates and eigenvalues of H with no time-step error.

Diffusion Monte Carlo,[26–29] on the other hand, is a guided random-walk relaxation technique which involves simulating the imaginary-time Schrödinger equation for the function $f=\psi_T\psi$. Here ψ_T is a trial importance sampling function which guides the random walk into the regions of highest amplitude. Specifically, an ensemble of replicas of the electron in the static solvent configuration is established. A short-time approximation is used which specifies that each replica is first allowed to diffuse through space, modeling the kinetic-energy term, then drift with constant instantaneous drift velocity $\nabla \ln \psi_T$ under the influence of the importance sampling function. The extent of these moves is governed by the time step, $\Delta\tau$. Finally, ensemble members are replicated or removed from the ensemble according to their values of the local energy $E_{\rm loc}=H\psi_T/\psi_T$ with probability: $\exp[-(E_{\rm loc}-E_{\rm ref})\Delta\tau]$. Here $E_{\rm ref}$ is a reference energy which is dynamically adjusted to keep the overall ensemble population stable at some finite normalization value. The long-time limit of this process becomes ground state dominated and reaches an equilibrium distribution of the replicas.

The electron ground-state properties are sampled after the DMC calculation has reached equilibrium. The distribution function of the electron replicas in the DMC calculation, $f_0(\mathbf{r})$, and can be expressed as

$$f_0(\mathbf{r})=\frac{1}{N_\tau}\sum_{k=1}^{N_\tau}\frac{1}{N_k}\sum_{i=1}^{N_k}\delta(\mathbf{r}_i-\mathbf{r}), \tag{2.1}$$

where N_τ is the number of time steps sampled after equilibrium (we used 12 000) and N_k is the number of replicas in the kth time step. The electronic ground-state wave function is $\psi_0(\mathbf{r})=f_0(\mathbf{r})/\psi_T(\mathbf{r})$, where $\psi_T(\mathbf{r})$ is a nonnegative analytical function. In this problem, the positions of the electron replicas are recorded in a three-dimensional histogram giving a discrete representation of the wave function.

In DMC the expectation value of any operator $\hat{A}$ can be determined from

$$\int\psi_0(\mathbf{r})\hat{A}\psi_0(\mathbf{r})d^3\mathbf{r} =2\left\langle\frac{\hat{A}\psi_T(\mathbf{r})}{\psi_T(\mathbf{r})}\right\rangle_{f_0(\mathbf{r})}-\left\langle\frac{\hat{A}\psi_T(\mathbf{r})}{\psi_T(\mathbf{r})}\right\rangle_{\psi_T^2(\mathbf{r})} +\int u(\mathbf{r})\left[\hat{A}-\left\langle\frac{\hat{A}\psi_T(\mathbf{r})}{\psi_T(\mathbf{r})}\right\rangle_{f_0(\mathbf{r})}\right]u(\mathbf{r})d^3\mathbf{r}, \tag{2.2}$$

a new result derived for the first time in the Appendix. Here, $u(\mathbf{r})=\psi_0(\mathbf{r})-\psi_T(\mathbf{r})$ is the difference between the normalized ground state and the trial wave function. $\langle[\cdots]\rangle_{f_0}$ denotes the average over $f_0(\mathbf{r})$ and is evaluated directly from DMC.[14,15] The second term on the right-hand side of the above equation is evaluated in the variational calculation. The last term is numerically integrated on the grid used for $\psi_0(\mathbf{r})$. In the case when ψ_0 is very close to ψ_T, the last term is of order smaller than $O[u^2(\mathbf{r})]$.

The electronic ground-state energy can be directly sampled from DMC as

TABLE I. DMC importance function parameters for xenon.

	a	b
Thirumalai	2.2	27.2
Fitted	4.8	24.0

$$E_0=\left\langle \frac{H\psi_T(\mathbf{r})}{\psi_T(\mathbf{r})} \right\rangle_{f_0}. \tag{2.3}$$

The choice of trial wave function $\psi_T(\mathbf{r})$ determines the magnitude of the time step $\Delta\tau$ and the rapidity with which the simulation converges to the true answer. The closer $\psi_T(\mathbf{r})$ is to the true electron ground-state wave function, the smaller will be the variation of $H\psi_T(\mathbf{r})/\psi_T(\mathbf{r})$ as a function of the electron position and the more efficient and accurate will be the importance sampling algorithm.[30] We used a pair product form for $\psi_T(\mathbf{r})$ for all of the pseudopotentials,

$$\psi_T(\mathbf{r})=\prod_{i=1}^{N} h(|\mathbf{r}-\mathbf{R}_i|), \tag{2.4}$$

where $\mathbf{R}_i$ is the position vector of fluid atom i and

$$h(r)=\exp[-ab/r(r^3+b)]. \tag{2.5}$$

Here a and b are variational parameters which give the lowest electron energy. The quantity $\langle \hat{A}\psi_T/\psi_T\rangle_{\psi_T^2}$ was integrated by three-dimensional quadrature. We find that a trial wave function of this form itself yields variational energies which are less than 10% higher than the exact DMC ground-state energy. The worst situation occurs in helium when the electronic ground state is localized. The agreement is especially good when the electron wave function is almost uniform in the simulation cell (for Xe at $\rho^*=0.7$, the trial energy are within 2% of the DMC value). Values of the variational parameters are summarized in Table I.

The DMC approach has the advantage of not requiring spatial discretization to compute ground-state energies and can be readily applied to larger and more complex systems. The accuracy and precision of these calculations is limited only by the short-time approximation and statistical uncertainties. As discussed above in connection with Eq. (2.2), expectation values other than the energy can only be obtained if the wave function can be represented on a grid and only the last term in this equation, which is itself small, is subject to grid discretization errors. In contrast, the errors in the FFT block Lanczos method are due to the spatial resolution of the wave function represented on a discrete grid without errors due to a finite time step and without statistical uncertainties. In problems where the potential function is rapidly varying in space DMC is preferable to FFT block Lanczos since one can improve DMC by decreasing the time step—a remedy easily achieved—whereas for rapidly varying potential functions FFT block Lanczos requires a fine spatial grid and can be expensive. DMC can also run into problems with rapidly varying potentials unless a good trial function such as the one used here is available. In the usual DMC methodology the E_{ref} estimator will fluctuate wildly in systems where the potential changes rapidly if a bad importance function is used and then there will be large statistical uncertainties. In the calculations described below the DMC was more accurate than the FFT block Lanczos by at best an order of magnitude.

The FFT block Lanczos method can be employed to obtain excited states. The excited-state method of Ceperley and Bernu[31] can be implemented to obtain excited states from DMC calculations, but due to the complexity in our ground-state wave functions this was not done here.

All of our calculations involve use of fluid samples with 256 or 864 particles in a minimum imaged cube with periodic boundary conditions. Ground-state electronic properties of 2048 particle systems were also computed and found to agree well with those of the smaller system. Interestingly, in xenon and argon, excited-state eigenvalues show system size dependence which is not converged in even the largest systems examined (2048 particles). Excited-states energies appear in "bands" with a characteristic number of excited states in each grouping, and characteristic energy gaps between bands. The ground-state eigenvalue is insensitive to system size as the ground-state energies in our periodic samples of highly polarizable noble-gas fluids behave similarly to that of a particle in a periodic box, which has no zero-point energy, and is the same for each system size. The excited-state energies, on the other hand, are box size dependent, leading to the size dependence of excited-state energies of our fluid samples. This behavior will be further investigated in a subsequent publication.[32] In contrast, for a system like helium, which has highly localized eigenstates, the densities of states for a 256-particle and 864-particle system are virtually identical.

The equilibrium neat fluid configurations were generated with standard constant-temperature molecular-dynamics methods, and the atom–atom interaction was taken to be a LJ potential with parameters $\sigma_{\text{Xe}}=4.0551$ Å, $\epsilon_{\text{Xe}}=229$ K, $\sigma_{\text{Ar}}=3.405$ Å, $\epsilon_{\text{Ar}}=119.8$ K, $\sigma_{\text{He}}=2.556$ Å, and $\epsilon_{\text{He}}=10.22$ K. The neat fluid configurations chosen were separated by sufficient time to insure statistically independence. For each solvent configuration, the ground-state energy was calculated with electron–atom pseudopotentials truncated at r_c. All reported electronic energies include a long-range correction based on a perturbation theory breakup of the potential in which we write the Hamiltonian as

$$H=-\frac{\hbar^2}{2m}\nabla^2+V_0+V_1,$$

where V_0 is the truncated potential with which we do our numerical simulations finding the eigenstates of $H_0=-(\hbar^2/2m)\nabla^2+V_0$ and V_1 is the part of the potential beyond r_c. We approximate the long-range correction as

$$\langle\psi|V_1|\psi\rangle=\int_{r_c}^{\infty} 4\pi r^2 dr\,\rho V\sim -2\pi\alpha\rho f_L/r_c$$

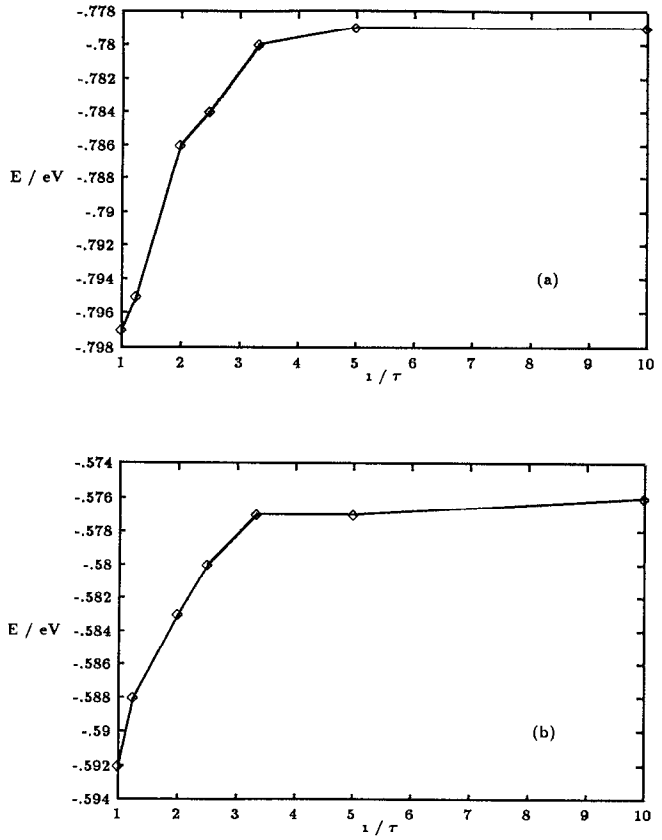

FIG. 1. The convergence of DMC vs time step for Xe at $\rho^*=0.5$ with the bare fitted pair pseudopotential (a) and the fitted potential including mean-field many-body polarization (b).

for our modified mean-field polarization potential discussed in Sec. III. Results obtained with this approximate long-range correction are insensitive to the truncation radius beyond $r_c = 2.5\sigma$ for densities lower than 0.7 but for higher densities $r_c = 3.5\sigma$ was taken for the many-body polarization models.

For each fluid density and pseudopotential, we took the best variational parameters for the trial wave function in our DMC calculations and tested the convergence with time step. For the pair and mean-field many-body polarization potentials (see Sec. III) at $\rho^*=0.5$ in Xe, the DMC converges at $\Delta\tau=0.2$ a.u. with a precision and accuracy of 0.2% as shown from Fig. 1. Typical DMC runs involved using 500 replicas and averaging results for 10 000 steps.

Details of the FFT BLD calculations were as presented in our previous studies.[33,34] Convergence of these calculations with grid size was tested with grids of 32^3 and 64^3 uniformly spaced points filling our simulation box. In an 864-particle fluid xenon sample at $\rho^*=0.9$ and $T=309$ K using the bare Thirumalai pair pseudopotential to be discussed in the next section, we obtained ground-state energies of $E_0^{32} = -1.277$ eV and $E_0^{64} = -1.254$ eV, respectively. The 64^3 grid result is in close agreement with the DMC result, using a time step $\Delta\tau=0.05$ a.u. and the same solvent configuration, we obtained $E_0^{\mathrm{DMC}} = -1.260 \pm 0.001$ eV.

TABLE II. Convergence and configurational variance of ground-state energies with the Kestner *e*–helium pseudopotential.

	Grid size		
ρ^*	16^3	32^3	64^3
0.3	0.780 38	0.853 43	0.856 57
0.3			0.862 12
0.3			0.938 62
0.5	1.469 4	1.641 5	1.641 9
0.5			1.858 9
0.5			1.572 8
0.7	2.969 1	3.156 5	3.163 2
0.7			2.934 2
0.7			3.068 1

In Table II we present results which indicate convergence of our electron–helium ground-state energies with grid size. A system of 864 particles was considered here. We see that our results are well converged across the entire range of fluid densities with 32^3 grid points. The table also summarizes results for different fluid configurations and we see that the fluctuations in ground-state energy with fluid configuration are on the order of 5%–10% in helium with the largest fluctuations occurring at a solvent density of $\rho^*=0.5$.

Table III shows similar grid-size convergence results in fluid xenon. The energies on a 64^3 grid in helium are better converged than in xenon at the same reduced density due to the difference in box sizes for the two systems. The box length L is directly proportional to the Lennard-Jones diameter σ_{LJ} for the same particle number and reduced density, namely $L = \sigma_{\mathrm{LJ}}(N/\rho^*)^{1/3}$, while the Lennard-Jones interaction diameter for helium is 63% of that for xenon. If we assume that convergence is determined by the number of grid points per ångstrom and that the electron–solvent potential in helium and in xenon are comparable in "smoothness," the convergence in helium with a 32^3 grid should be roughly comparable to that of a 64^3 grid in xenon for the same number of particles and reduced density. The helium eigenvalues were shown to be converged to within 0.2% or less in Table II. A test was also performed on a 256-particle xenon system with $\rho^*=0.5$ and a 64^3 grid. Reducing the system size to this extent improves the discretization in each dimension by a factor of 1.5. The resulting eigenvalue differed by only 0.5%, further confirming that the BLD results are free from any significant discretization error. Also, we find that the variation in

TABLE III. Convergence and configurational variance of ground-state energies with an Xe fitted potential with mean-field polarization.

	Grid size	
ρ^*	32^3	64^3
0.5	−0.5735	−0.5654
0.5	−0.5733	−0.5652
0.7	−0.6581	−0.6443
0.7	−0.6576	−0.6465

ground-state energy with configuration is only a few tenths of a percent for the ground states of fluid xenon configurations.

III. ELECTRON–SOLVENT INTERACTION POTENTIALS

A variety of electron–atom pseudopotentials were used in our calculations of the excess electronic states of simple atomic fluids. In this section we discuss these pseudopotentials and demonstrate the nonuniqueness of the pseudopotential approach by showing that vastly different pseudopotentials can give very similar gas-phase electron–atom scattering data. In later sections we will find that very different pseudopotentials give very similar bulk phase electronic properties as well.

The electron–atom bare pair potentials we have treated in our calculations have the general form

$$V_{e\text{-}X}(r)=V_r(r)+V_p(r). \tag{3.1}$$

Here $V_r(r)$ is the short-range repulsive component of the pseudopotential which incorporates terms representing the interaction of the incoming electron with the static charge distribution of the target atom as well as terms accounting for exchange and orthogonality of the incoming electron wave function with the wave functions of the target atom electrons. The second term $V_p(r) = -\alpha e^2 S(r)/2r^4$ represents the charge–induced-dipole polarization interaction. Here α is the atomic polarizability and $S(r)$ is a switching function which accounts for the fact that as the electric field from the incoming electron penetrates the charge distribution of the target atom it is screened by this charge distribution.

In fluids of highly polarizable atoms such as argon and xenon, the long-range charge–induced-dipole polarization interaction cannot, in general, be treated in terms of a simple sum of pairwise additive terms such as $V_p(r)$. Under these circumstances the local electric field which induces the dipole in molecule i is the superposition of the Coulomb field from the excess electron and the electric fields due to all the other induced dipoles, thus

$$\mathbf{E}_i=\mathbf{E}_i^{(0)}+\sum_{k\neq i}^{N}\alpha_k\mathbf{T}_{ik}\cdot\mathbf{E}_k, \tag{3.2}$$

where the direct electric field at $\mathbf{r}_i$ due to the charge at the origin is $\mathbf{E}_i^{(0)}=e\hat{\mathbf{r}}_i S^{1/2}(r_i)/r_i^2$ and $\mathbf{T}_{ik}=(3\hat{\mathbf{r}}_{ik}\hat{\mathbf{r}}_{ik}-\mathbf{1})/r_{ik}^3$. The fact that the dipole induced in a given atom $\mu_i=\alpha_i\mathbf{E}_i$ depends on the fields of all the other induced dipoles gives rise to a set of $3N$ coupled linear equations for the induced dipoles which can be solved self-consistently. The many-body electrostatic polarization energy of the condensed system is thus obtained as the energy of all the induced dipoles in the direct electric field of the charge,

$$V_p^{\mathrm{MB}}(\mathbf{r}^{3N})=-\frac{1}{2}\sum_{i=1}^{N}\mu_i\cdot\mathbf{E}_i^{(0)}. \tag{3.3}$$

For a system with N polarizable solvent atoms, a $3N\times 3N$ matrix equation must be inverted in order to evaluate the many-body electron–solvent polarization potential. For a fixed solvent configuration the direct inversion of the matrix is efficient since it only needs to be performed once. When the configuration is sampled many times a self-consistent iteration approach can be used to minimize the computational effort in solving this large system of equations (3.2).

Calculation of the many-body polarization interaction as discussed above is computationally intensive. If it is assumed that the solvent structure is unperturbed by the excess electron, a mean-field approach to this problem[16] can considerably simplify these calculations. This approach involves the assumption that the local field which includes the effect of other induced dipoles points in the same direction as the direct electric field but with a magnitude modified by a distance-dependent screening function $f(r)$. Thus,

$$\mathbf{E}_i(\mathbf{r}_i)=\mathbf{E}_i^{(0)}(\mathbf{r}_i)f(r_i)=e\hat{\mathbf{r}}_i S^{1/2}(r_i)f(r_i)/r_i^2.$$

With this model one can compute the component of the local field along the distance vector between an atom and the electron in the presence of a continuous fluid of dipoles distributed according to the unperturbed fluid pair correlation function $g(r)$. The final result is a self-consistent integral equation for $f(r)$ dependent only on the unperturbed fluid structure[16] which we can solve numerically

$$\begin{aligned}S^{1/2}(r)f(r)=S^{1/2}(r)f(r)+\pi\rho\alpha\int_0^\infty ds\,g(s)s^{-2}\\ \times\int_{|R-s|}^{|R+s|}dt\,S^{1/2}(t)f(t)t^{-2}\\ \times\left[\frac{3}{2s^2}(s^2+t^2-r^2)(s^2+r^2-t^2)\right.\\ \left.+(r^2+t^2-s^2)\right].\end{aligned} \tag{3.4}$$

This approximation allows one to express the potential energy including the many-body nature of the polarization interaction as a sum of two-body terms. The many-body, self-consistent field problem is thus reduced to a mean-field, density-dependent, pair potential of the form $V_{\mathrm{MF}}=V_r(r)+V_p(r)f(r)$.

The average local field function $f(r)$ for xenon at several different solvent densities is presented in Fig. 2. These functions decay from unity to the Lorentz local-field factor f_L in an oscillatory fashion due to the local structure of the fluid. The factor f_L depends on the density of polarizable centers, ρ, and has the form $f_L=[1+(8/3)\pi\rho\alpha]^{-1}$. For comparison, the value of f_L at the high fluid density of $\rho^*=0.7$ in helium is only $f_L=0.93$ so we ignore these local-field screening effects in all our condensed-phase helium calculations (for xenon at $\rho^*=0.7$, $f_L=0.74$).

These results for $f(r)$ indicate that the self-consistent mean-field potentials will be more weakly attractive than the pair polarization potential. Physically, this is due to the effect of the repulsive induced-dipole–induced-dipole interactions on the electric field. These interactions make it unfavorable to have large induced dipoles. Again, in the mean-field treatment this is reflected by a simple reduction

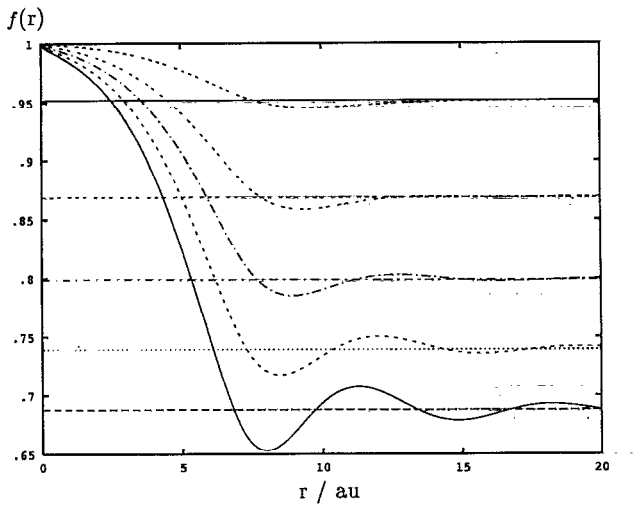

FIG. 2. Self-consistent mean-field screening functions for the electron–xenon system at densities $\rho^*=0.9$, 0.7, 0.5, 0.3, and 0.1 and temperature $T=309$ K. The curve for the highest density-state point has the lowest asymptotic value, and the asymptotic values increase monotonically to one with decreasing density.

in the magnitude of the induced dipole which is assumed to be pointing in the direction of the direct electric field.

We expect that the mean-field theory will work best for excess electrons in unperturbed neat fluids. When the solvated excess electrons (i.e., fully equilibrated) significantly perturb the fluid structure as in helium or polar solvents such as water or ammonia, an altered mean-field equation may be required.

A. *e*–helium pseudopotentials

New pair pseudopotentials for the electron–helium interaction were constructed using a simple exponential repulsive component $V_r(r) = A\exp(-\beta r)$ and a polarization switching function of the form $S(r) = r^4/(r^2+d^2)^2$ to give $V(r) = V_r(r) - \alpha S(r)/2r^4$. The atomic polarizability of helium was taken to be $\alpha=1.3834$ a.u.[3] and the parameter in the polarization switching function was taken to be $d^2 = 0.7$ a.u.[2]. The other two parameters in the pseudopotential, A and β, were then adjusted to give agreement with $l=0$ phase shift data obtained from various sources. These parameter values are listed in Table IV. Phase shifts calculated using various pseudopotentials and those obtained from *ab initio* calculations which reproduce experimental cross-section data are compared in Fig. 3(a). Here we present two sets of phase shifts to which potentials were fitted: one due to McEacharan and Stauffer,[35] and the second set due to Williams.[36] We see that these results are reasonably close at low k and deviate by about 4% at the highest wave vectors considered. We shall see shortly that these slight differences in phase shifts can result in substantial qualitative differences in the fitted potentials. Phase shifts for the potential due to Rama Krishna and Whaley[37] and the results of Nesbet[38] to which this potential was fitted are also presented in this figure. We see that the fitted phase shifts lie within the two sets discussed above. Figure 3(a) also presents the phase shifts calculated for the pseudopotential developed by Kestner *et al.*[39,3] We see that

TABLE IV. *e*–He pseudopotential parameters in atomic units.

Depth (eV)	A	β
−0.0175	17.832	2.15
−0.0325	49.76	2.6

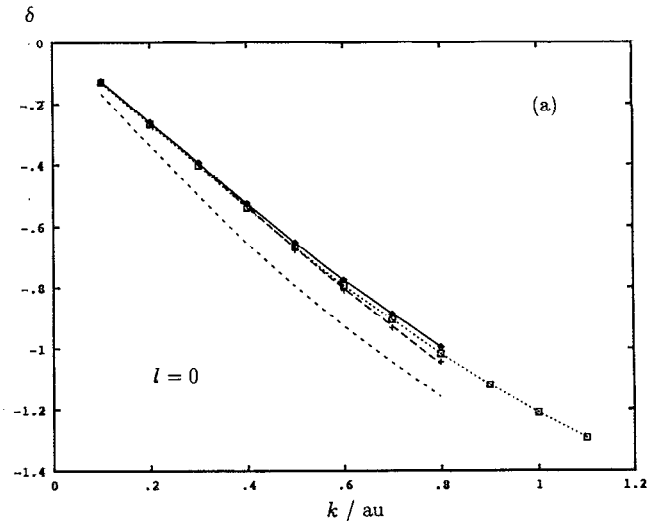

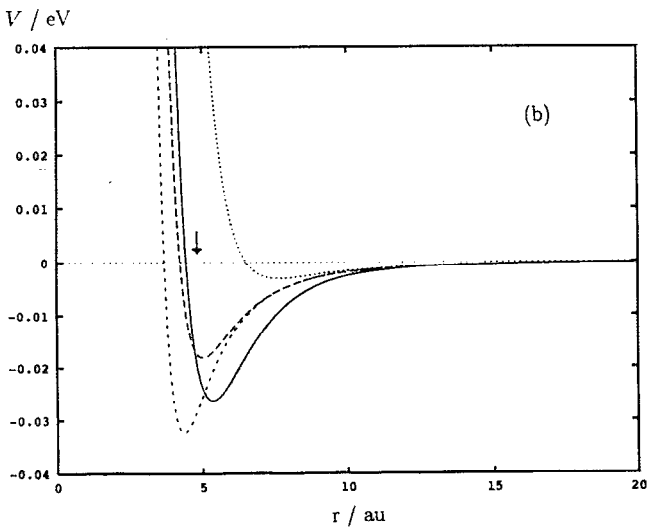

FIG. 3. (a) $l=0$ electron–atom scattering phase shifts for helium. The curves are results calculated with various pseudopotentials and the points are data from *ab initio* calculations; diamonds, Ref. 36; pluses, Ref. 37; squares, Ref. 39. The dashed curve which does not go through any of the sets of points denotes the phase shifts obtained with the pseudopotential due to Kestner *et al.* (Ref. 39). (b) Pseudopotentials for the electron–helium system. The solid curve is potential due to Rama Krishna fitted to Nesbet phase shifts, the long-dashed curve is the potential form we have fitted to McEacharan–Stauffer phase shifts, the short dashed curve is the potential form we have fitted to Williams phase shifts, and the dotted curve is the pseudopotential due to Kestner *et al.* For comparison, the arrow indicates the atom–atom interaction diameter.

TABLE V. *e*–Ar pseudopotential parameters in atomic units.

Depth (eV)	A_1	β_1	A_2	β_2
1.0	−31.6712	1.789 84	127.081	2.2
0.78	−35.3910	1.655 38	85.4794	1.9
0.60	−36.5322	1.465 49	61.6499	1.6

this pseudopotential gives phase shifts which are typically about 10% below those of the potentials discussed above.

The pseudopotentials mentioned above are displayed in Fig. 3(b). We see quite considerable variation in both well depth and interaction diameter.

B. *e*–argon pseudopotentials

The form of the pseudopotential used to describe the electron–argon interaction involves a repulsive component $V_r(r) = \Sigma_{i=1}^{2} A_i \exp(-\beta_i r)$ combined with the same polarization potential and switching function discussed above for helium. The value of d^2 was again taken to be 0.7 and the polarizability of argon was taken to be $\alpha = 11$ a.u.[3]. Three different parametrizations for V_r with increasing strength of repulsion were fit to the phase shifts and are summarized in Table V. The phase shifts calculated with these pseudopotentials are presented in Fig. 4(a). In Fig. 4(b) we present these different bare pair potentials together with their associated density-dependent self-consistent mean-field pair potentials. Again, we see that slight differences in the quality of the fit to the phase shifts lead to considerably different pseudopotentials. Interestingly, the differences between the density-dependent potentials for a given potential form are quite small compared with the gross differences we see between one potential form and another. We shall see in Sec. IV that these apparently subtle changes in the effective potential with density have a profound influence on the calculated ground-state energy values. Remarkably, the gross differences from one potential form to another have little effect on the calculated ground-state energies provided the potential form makes physical sense and gives a good representation of the phase shifts.

C. *e*–xenon pseudopotentials

We have considered two pseudopotential forms in our studies of excess electrons in xenon. These have the usual attractive polarization ($\alpha = 27.09$ a.u.[3]) form discussed above and include a slightly more complicated switching function due to Temkin and Lauskin

$$S(r) = 1 - A \exp(-2x) \sum_{n=0}^{5} a_n x^n, \tag{3.5}$$

where $x = (9/2\alpha)^{1/4} r$ and the other constants are summarized in Table VI.

The potentials differ only in the short-range repulsive part of the interaction. The first potential is a form in which the parameters have been optimized to reproduce *s*-wave phase shifts and it has the form

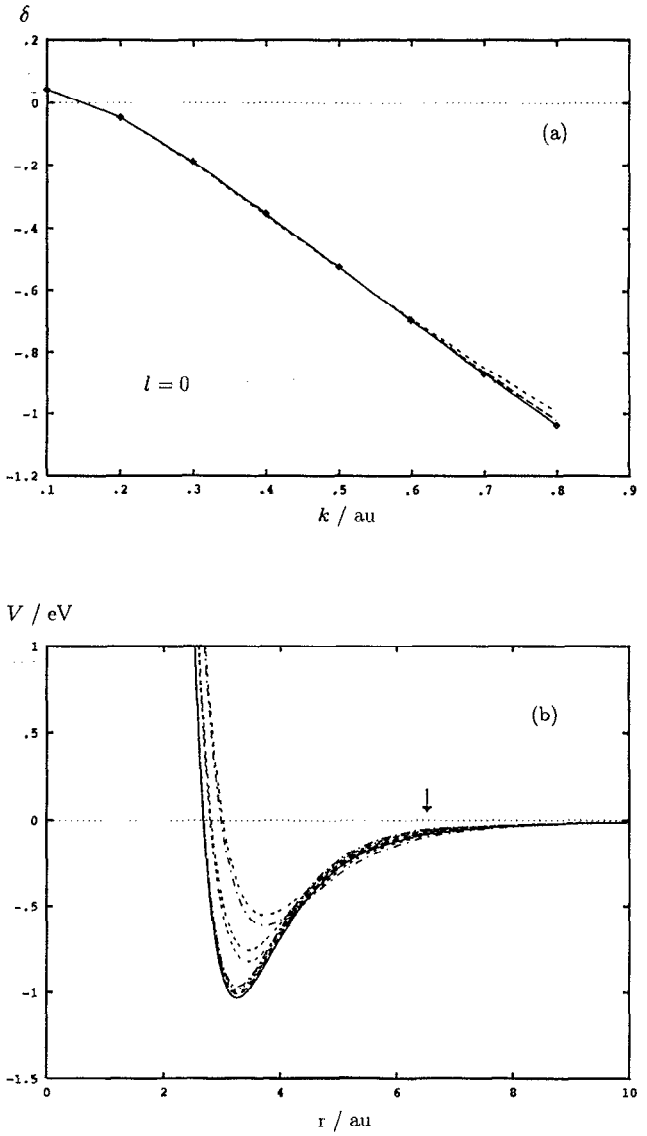

FIG. 4. (a) $l=0$ electron–atom scattering phase shifts for argon. The points are data from *ab initio* calculations (Ref. 53). The curves are results obtained with various fitted pseudopotentials; the solid curve shows results with the deepest pseudopotential; the long-dashed curve, intermediate depth potential; and short-dashed curve, shallowest potential. (b) Various sets of density-dependent mean-field self-consistent polarization potentials for the electron–argon interaction. For the deepest set of curves we display potentials for densities of $\rho^* = 0.1$, 0.3, 0.5, 0.7, and 0.9. For the other potentials we display only the extreme densities $\rho^* = 0.1$ and 0.9 (lowest and highest, respectively). The arrow indicates the atom–atom interaction diameter.

$$V_r^E(r) = \sum_{i=1}^{2} A_i \exp(-\beta_i r)$$

with parameters $A_1 = 128.237$, $\beta_1 = 1.900$, $A_2 = -18.091$, $\beta_2 = 1.355$. The second electron–xenon pseudopotential form we have used in our studies was developed by Thirumalai[40] and it has a repulsive component $V_r^A(r)$ which is derived from *ab initio* considerations and includes terms representing interactions with the static charge distribution of the xenon atom as well as exchange and correlation

TABLE VI. *e*–Xe polarization switch parameters in atomic units.

A	a_1	a_2	a_3	a_4	a_5
0.148 15	6.75	13.5	13.5	9.0	4.5

effects. This potential has a maximum value of about 30 eV at very small separations. We have used an infinitely repulsive form which was fitted to this potential around the region of the bowl and repulsive core in our previous path-integral calculations.[3] The infinitely repulsive form starts to deviate significantly from the Thirumalai pseudopotential above energies of about 10 eV. To check on the influence of these high-energy differences we have performed our ground-state energy calculations with both the fitted and full pseudopotentials and find no differences for these low-energy calculations across the whole fluid range of densities. Again, we see that these two-body potentials are qualitatively different from one another and the changes in the potential with density associated with the mean-field treatment of many-body polarization are comparatively small.

Phase shifts calculated with these pseudopotentials are compared with theoretical *s*-wave phase shifts in Fig. 5(a). The Thirumalai potential does not reproduce the *s*-wave phase shift as well as the fitted pseudopotential. The two potentials and their families of density-dependent, mean-field, many-body polarization potentials are compared in Fig. 5(b).

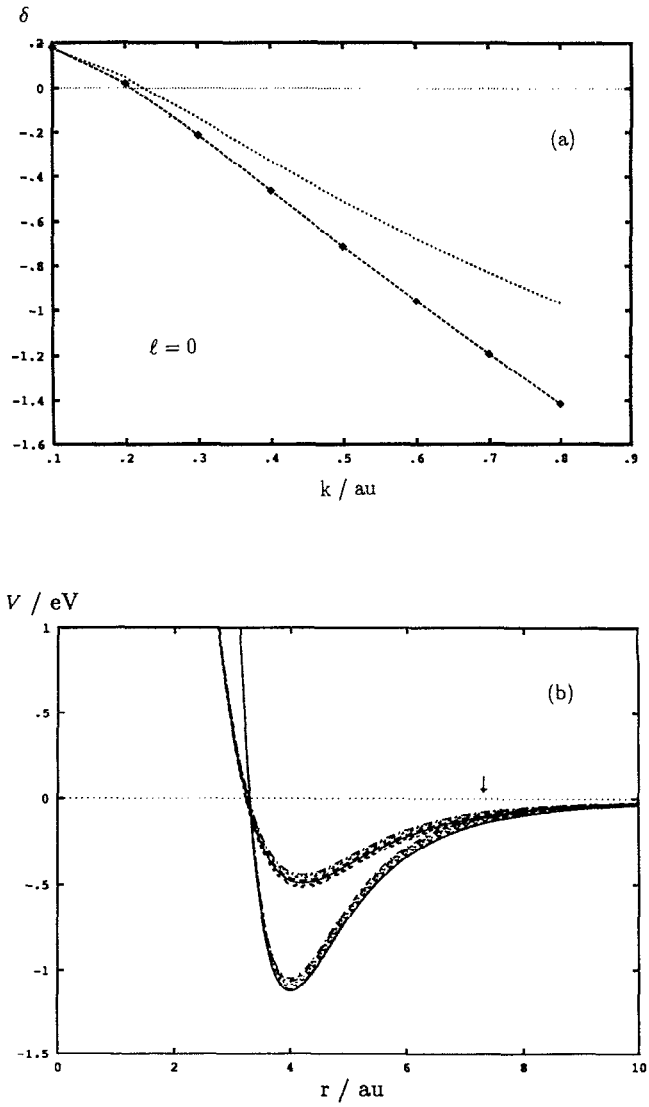

FIG. 5. (a) $l=0$ electron–atom scattering phase shifts for xenon. The points are data from *ab initio* calculations (Ref. 54). The dashed curve through these points shows results obtained with our fitted pseudopotential; the dotted curve shows results obtained with the Thirumalai potential. (b) Various sets of density-dependent self-consistent polarization potentials for the electron–xenon interaction. The deepest set of curves is obtained from the fitted form and the shallower set is derived from the Thirumalai form. The lowest curve of each set is the bare pair potential and the higher curves are at higher densities of $\rho^*=0.1$, 0.3, 0.5, 0.7, and 0.9, respectively. The arrow indicates the atom–atom interaction diameter.

IV. RESULTS

A. Helium

In Fig. 6(a) we present our calculated ground-state energies as a function of density in fluid helium along the supercritical isotherm at $T=50$ K. Experimentally, it is found that the V_0 values are insensitive to temperature,[41] so we might expect a similar insensitivity for the ground-state energies. Results are compared for the various pseudopotentials discussed in Sec. III. We see that the pseudopotential of Kestner *et al.*[39,3] which, as seen in the preceding section, does the poorest job of reproducing the phase shifts, gives ground-state energies that are close to the experimental V_0 values.[41–45] Both the potential presented by Rama Krishna[37] and the form we give in Sec. III give ground-state energy results which lie below the experimental V_0 values across the entire density range. For these potentials which reproduce the phase shifts we see that, despite the fact that there are considerable differences in pseudopotential well depth and interaction diameter, these potentials all give very similar ground-state energy results. This occurs due to cancellations between the kinetic and potential components of the total energy as we discuss in Sec. IV B.

In Fig. 6(b) we present 50% isosurfaces of the ground-state excess electronic density of representative fluid configurations at various solvent densities. The gross features of these isosurfaces are fairly insensitive to the particular form of the potential used. We see that the ground excess electronic states of these unperturbed helium configurations are all quite strongly localized in small cavitylike density fluctuations in the fluid. Space and Coker[34] have recently used their nonadiabatic dynamics methods to model the relaxation and dynamical trapping processes which occur when electrons are injected into these localized cavity states of unperturbed fluid configurations. States as strongly localized as this are generally nonconducting, consequently we expect these ground-state energy values to lie below the conduction-band energies as we find is indeed the case for all the pseudopotentials which give

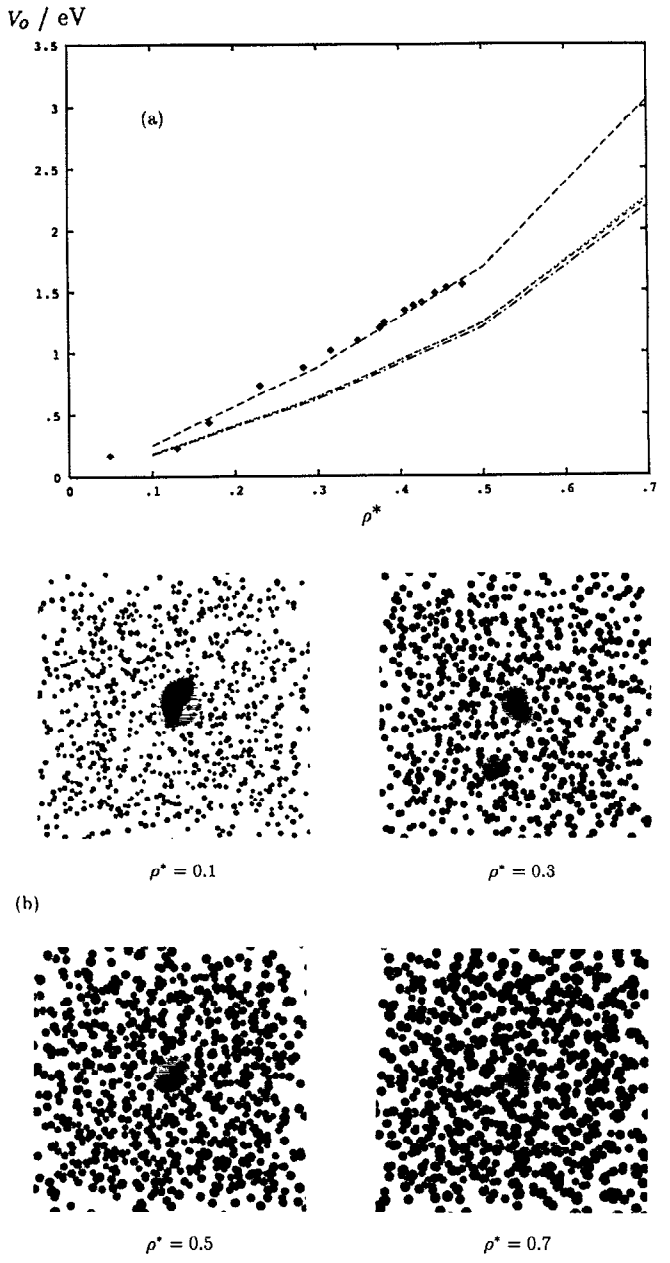

FIG. 6. (a) Excess electronic energies in helium. Experimental V_0 results are displayed as diamonds. Calculated ground-state energies: E_0 are displayed as curves. The long-dashed curve is obtained using the pseudopotential due to Kestner *et al.* (Ref. 39). The short-dashed curve is obtained with the pseudopotential fitted to McEachran–Stauffer phase-shift data. The dotted curve is obtained with the pseudopotential fitted to Williams phase-shift data. The dash-dotted curve is obtained with the Rama Krishna potential. (b) Representative configurations of the electron–unperturbed fluid helium system at various solvent densities. Atoms are represented as spheres with radii equal to 20% of the Lennard-Jones helium–helium interaction diameter, σ. The electron is represented by an isosurface on which the ground-state electron density has 50% of its maximum value.

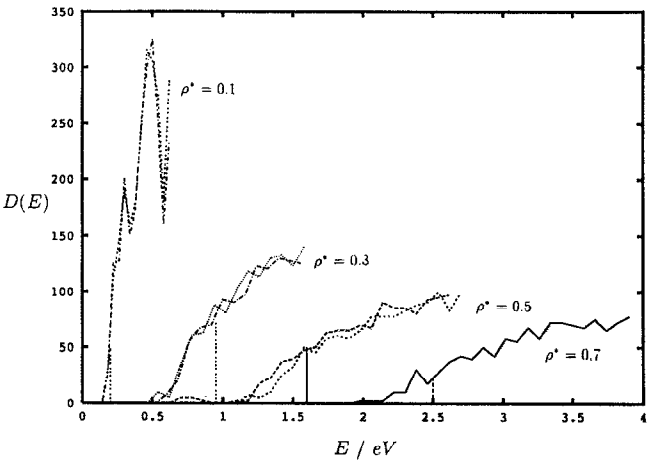

FIG. 7. Density of excess electronic states in fluid helium at various solvent densities. Vertical lines indicate experimental conduction-band energies V_0 (Refs. 41–45). The two curves at $\rho^*=0.1$ are at temperatures $T=50$ K (dotted curve) and $T=309$ K (dash-dotted curve). All other curves are for $T=50$ K. Curves at $\rho^*=0.3$ are for the electron equilibrated fluid (dotted curve) and unperturbed fluid (dash-dotted curve). Similarly at $\rho^*=0.5$ the electron equilibrated fluid (dashed curve) and unperturbed fluid (dotted curve) results are presented.

accurate phase-shift data. The Kestner potential,[3,39] which does not reproduce the phase shifts, is thus somewhat unphysical as it gives localized nonconducting ground states whose energies are equal to, or higher than the experimental conduction-band energies. We see that the ground-state energies calculated for the accurate pseudopotentials all asymptotically tend to the V_0 values at low densities, indicating that the gap between the ground state and lowest-energy conducting state gets smaller as the density is decreased.

As the helium density is increased we see that the ground-state energies increase monotonically. Since the electron–helium and helium–helium interaction diameters are comparable [see Fig. 3(b)], when the atoms forming the walls of the ground state solvent cavity are in close contact, the electron–solvent interaction will be dominated by the repulsive core of the electron–solvent pseudopotential. As the solvent density is increased the average unperturbed solvent cavity size will decrease giving increased localization of the electronic states and a higher kinetic energy. The smaller the average size of the cavities, the more the harshly repulsive core of the pseudopotential is sampled, and the higher will be the total potential energy.

In an attempt to understand the factors which influence the onset of electronic conduction in fluid helium we have used our block Lanczos diagonalization method to compute the density of excess electronic states at various solvent densities. These results are presented in Fig. 7 and were obtained by binning the energies of the first 100 eigenstates, averaged over five different equilibrium fluid configurations. A regular grid of 32^3 points throughout our simulation cell was used in these calculations. We have performed this calculation with both our fitted potentials, and the Rama Krishna form and almost identical results were obtained. The density of states obtained with the Kestner potential is very similar in shape to these other potentials but it is offset in energy by a constant corresponding to the difference in the ground-state energies. At low solvent densities, the initial rise of the density of states

is very rapid. As the solvent density is increased, however, the low-energy tail of the density of states shows a more gradual increase with energy. This behavior can be understood in terms of the fact that the lowest-energy states of fluid helium generally involve the electron localizing in different size voids throughout the fluid. At lower solvent densities the voids are larger and all their state energies are smaller and more closely spaced so the state density increases very rapidly. At the higher solvent densities, on the other hand, the voids are smaller and there is thus a larger spread of electronic energies so the density of states increases more slowly.

Along the energy axis in this figure we have marked off the experimental conduction-band energies at the various solvent densities.[41–45] At the lowest solvent density the experimental conduction-band energy lies close to the bottom of the density of states. As the solvent density is increased, however, the conduction-band energy moves higher up into the broad low-energy tail of the density of states, well separated from the ground-state energy.

In Fig. 7 we compare densities of states for fluid samples which have been equilibrated in the presence of the electron and those for neat fluid samples at solvent densities of $\rho^*=0.5$ and $\rho^*=0.3$. The main difference between the equilibrated and neat densities of states at $\rho^*=0.5$ is the presence of a distinct ground-state band associated with s-like states in large equilibrated solvent cavities, separated from the excited-state band by about 0.2 eV. The low-energy tail of the excited-state band of the equilibrated fluid density of states and the neat fluid band edge start at very similar energies. The value of the state density for the equilibrated fluid in the region of the low-energy tail, however, lies above that of the neat fluid due to increased state density associated with the p-like states supported by the larger equilibrated solvent cavity. These differences between equilibrated and neat fluid samples are less pronounced at the lower solvent density.

In fluid helium we generally see states which are localized on the length scales of our simulation cells with perhaps the exception of the lowest solvent density $\rho^*=0.1$. Space and Coker[32] have studied the density of states in fluid argon and xenon where, as we shall see in the next section, the states are highly extended on the length scales of a simulation cell. They find that the densities of states become strongly spiked at various solvent densities as a result of box quantization. Due to the use of periodic boundary conditions, the calculated excess electronic state energies cluster in bands giving rise to the spikey density of states when the states are extended on the length scale of the simulation cell. We clearly see no evidence of this signature of extended states in our densities of states in helium at $\rho^*=0.3$ and 0.5. At $\rho^*=0.1$, however, we do see reproduceable spikes at higher energies in the density of states indicating the onset of extended excited states at this low density.

This raises questions concerning the validity of simple Wigner–Seitz–like models to describe the onset of conduction in fluids such as helium[7,10,8] at higher solvent densities. This model assumes that the solvent is composed of a regular array of scatterers, one occupying each Wigner–Seitz sphere. This regular array will support extended conducting states and by assuming that the wave function is, on average, radially symmetric around each solvent atom, the energy of the lowest state can be obtained by applying the boundary conditions that the wave function must vanish at the core of each solvent atom and that its slope should be zero at the edge of the Wigner–Seitz sphere. Clearly, this model says nothing of the disorder of the solvent which is ultimately responsible for the fact that the states in dense fluid helium are not extended. This model may provide a reasonable description of the situation in the low-density fluid where we see the signature of "macroscopically" extended states.

At $\rho^*=0.1$ we present densities of states for two temperatures $T=50$ K and 309 K, which reveals a negligible temperature dependence. Tests at higher density indicate similar insensitivity to temperature in the electron–helium system.

B. Xenon

In Fig. 8 we present the calculated ground-state energies of the excess electron as a function of density in fluid xenon. We have performed calculations both on the liquid–vapor coexistence curve where the experiments were performed, and on the 309 K isotherm. The ground-state energy results for these different slices through the phase diagram are indistinguishable. Figure 8(a) compares the ground-state energies for the density-dependent mean-field many-body polarization potentials for xenon presented in Sec. III with the experimental V_0 results.[1] Results obtained with the density-independent two-body potentials are presented in Fig. 8(b) to indicate the importance of many-body polarization effects.

Despite the dramatic differences between the pseudopotential fit to phase shifts and the Thirumalai pseudopotential (see Fig. 5), we see that both potentials give very similar ground-state energies; the two sets of values obtained with the density-dependent self-consistent polarization forms are always within a few percent of one another up to high fluid densities ($\rho^*\sim 1.0$). The two curves obtained when the many-body polarization effects are ignored agree up to $\rho^*\sim 1.0$, but at higher densities we see considerable deviations due to differences in the short-range repulsive parts of these potentials. Nevertheless, the relatively subtle differences between the different self-consistent polarization potentials for a given potential form have a profound effect on the ground-state energy curves. We see that when the many-body polarization effects are ignored the ground-state energy does not show an upturn until extremely high, unphysical densities (for the Thirumalai potential the ground-state energy still has not turned up by $\rho^*=3.0$). We have calculated the ground-state energies at these very high solvent densities for both glassy and crystalline states and find very little difference. When many-body polarization is ignored the ground-state energy obtained with the fitted potential has its minimum at about twice the density where the experimental V_0 values begin to upturn. However, when many-body effects are incorpo-

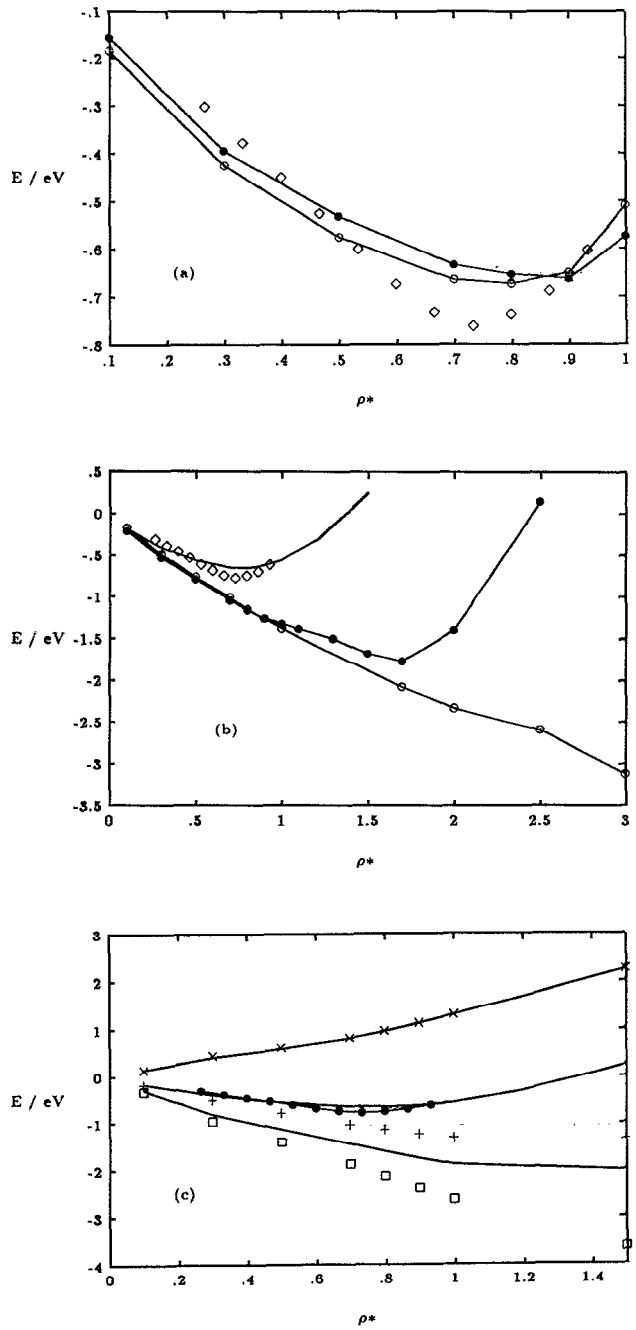

FIG. 8. Excess electronic energies in xenon. (a) Diamonds are experimental V_0 values (Ref. 1). Calculated ground-state energies obtained with mean-field many-body polarization potentials are given. Solid circles denote ground-state energies for the Thirumalai potential, and open circles denote results for the fitted potential form. (b) Diamonds are experimental V_0 values. The solid curve is the ground-state energy calculated using the mean-field many-body polarization potential (fitted form). Other curves are ground-state energy results obtained when the bare pair potentials are used, ignoring many-body polarization. Solid circles denote results with the bare fitted potential and open circles denote results obtained with the Thirumalai form. (c) Kinetic- and potential-energy breakup using bare and mean-field many-body polarization potentials for the fitted form. Squares are the average potential energy, (crosses) are the kinetic energy, and (pluses) are the total energies obtained for the bare potential. The lowest curve is the average potential energy obtained with the mean-field many-body potentials and the highest curve gives the kinetic energies obtained with these potentials. The middle curve is the total energy.

rated through self-consistent mean-field theory, the calculated ground-state energies show similar qualitative density dependence to the experimental V_0 values with the minimum density in comparatively close agreement with the experimental results [see Fig. 8(a)]. The calculated ground-state energy curves for both the fit potential and Thirumalai pseudopotentials (including the mean-field corrections) have a shallower density dependence and minima at slightly higher densities than the experimental conduction-band energy curve.

In Fig. 8(c) we also present the breakup of the total energy into potential and kinetic components computed using the fit potential. Results for both the bare pair form and mean-field many-body polarization potentials are presented. Interestingly, we find that the kinetic-energy curves for both the pair and many-body polarization potentials are in very close agreement and that the differences in the density dependence of the total energy result primarily from differences in the average potential energy. The upturn in the total energy obtained with the mean-field many-body polarization potential occurs at a density in close agreement with experimental V_0 values. The minimum occurs because the average potential energy levels off at high density, while the kinetic contribution continues to increase. For the bare pair potential we see that the average potential energy continues to decrease across the entire range of densities, even into the dense solid regime. Only at very high unphysical densities, where kinetic energy increases more rapidly than the potential decreases do we see a slight upturn with the bare pair potential form. The reason that the density dependence of the average kinetic energy is so similar for both the pair and mean-field many-body polarization potentials is probably due to the fact that the repulsive walls of the pair and density-dependent potentials are very similar [see Fig. 5(b)]. This means that the potentials have the same size cores, giving rise to about the same excluded volume and thus about the same kinetic energy.

In Fig. 9 we demonstrate that the agreement between the ground-state energies calculated using the Thirumalai and fit potential forms is far from coincidental. Rather, the agreement results from the almost exact cancellation of very different potential- and kinetic-energy contributions for the two different forms of the pseudopotential. From Fig. 5 we see that the fit potential is considerably deeper than the Thirumalai form. Thus from Fig. 9 where we present the breakup of the energies computed using the density-dependent pseudopotential, the average potential energy obtained using the fitted form is considerably more negative than that obtained with the Thirumalai form. The kinetic energy obtained with the fitted potential, however, is very much more positive than that found with the Thirumalai form. This is due to the fact that the harsh repulsive core of the fitted form is significantly larger than that of the Thirumalai form (see Fig. 5), so the "free volume" available to the electron in the fluid is much reduced when the fitted potential is used. Because the electron is confined in a smaller region of space, its ground-state wave function will vary more rapidly and gives it a larger kinetic energy.

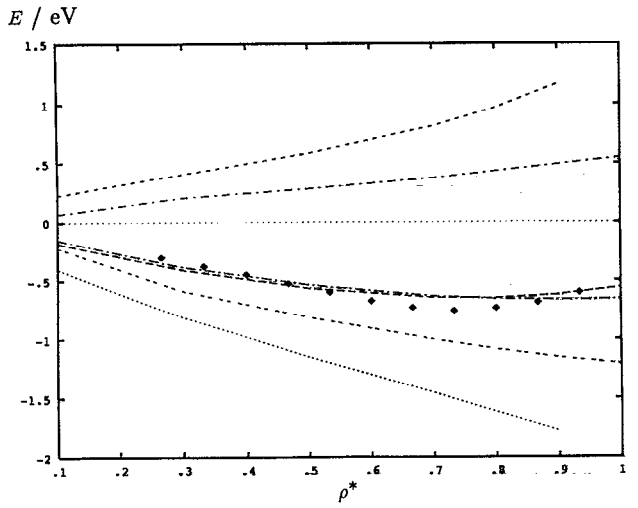

FIG. 9. Influence of the choice of pseudopotential on breakup of total ground-state energy into potential and kinetic components for electrons in xenon. Interactions represented using self-consistent mean-field density-dependent pair pseudopotentials. The two curves close to experimental values (diamonds) are the same total ground-state energies displayed in Fig. 8(a). Curves above zero are kinetic energies obtained with the Thirumalai potential (dash-dotted), and the fitted potential (short-dashed). The curves below the total-energy results are the electronic ground-state potential-energy values obtained with the Thirumalai (short-dashed–short-dashed) and the fitted potential values (dotted).

In Fig. 10(a) we present three-dimensional contour isosurfaces of the ground-state electron density. The contours correspond to the surfaces on which the electron density is roughly 50% of its maximum value. The wave functions were obtained using the mean-field many-body polarization and the potential fit to the phase shifts, but very similar contour surfaces are found when the Thirumalai pseudopotential is used. At lower solvent densities, $\rho^* \leqslant 0.3$ or 0.5, we see that the 50% contour of the ground-state electron density is confined to a small region of space and does not extend over our simulation box. The regions in which the electron density becomes concentrated correspond to solvent density fluctuations in which many atoms pack close enough that the attractive wells of the electron–atom pseudopotential overlap. In the lower-density parts of the fluid outside these regions, the attractive wells of the solvent atoms are further apart and do not overlap effectively. In terms of the lakes-to-oceans percolation ideas of Coker, Thirumalai, and Berne[3] and Stratt and coworkers,[22] we would call these states lakelike states.

As the solvent density is increased we see that the regions of fluid where the attractive wells overlap begin to spread throughout our fluid sample. Thus, at a reduced density of $\rho^*=0.7$ in xenon, we see that the ground-state electron density is almost uniformly distributed throughout our experimental fluid sample in a highly percolative oceanlike state.

As the density is increased beyond this point, the volume occupied by the repulsive cores of the electron–solvent pseudopotential begins to become more important than the volume occupied by the overlapping potential wells. The repulsive cores thus begin blocking off the formerly open channels through which the electron density once freely percolated. This causes the ground-state electron density to become fragmented. Here, we expect to observe states involving small lakes of electron density which may be connected by rivers. We see such states at the solvent densities of $\rho^*=0.9$ and 1.0 for example.

It should be noted that because we do all our calculations at the different densities with the same fixed number of particles (i.e., 864) the size of our simulation box shrinks as we increase the density. Consequently, the length scales of the images displayed in Fig. 10(a) are all different. For example, the length scale of the image at $\rho^*=0.3$ is actually about 1.5 times larger than that at $\rho^*=1.0$. These scale changes do not negate our comments concerning the variation of the spatial extent of the ground-state electron density with solvent density. If we look at a portion of the $\rho^*=0.3$ image containing the electron and about 2/3 the size of the full simulation cell, the resulting section of this image will be about the same physical dimension as the entire image displayed at $\rho^*=0.7$. We see that this portion of the $\rho^*=0.3$ image will still have large void regions surrounding the more localized electron density in contrast to the almost uniform distribution of electron density throughout the entire image at $\rho^*=0.7$. These scale changes in fact make our statements concerning the fragmentation of the electron density at high solvent densities even stronger for we are actually focusing on smaller regions of space. We see that the electron density becomes separated into many small regions which may or may not be connected by narrow riverlike passages through the fluid. Also, we have validated these results in studies on systems of 2048 particles and found good agreement.

To quantify the qualitative trends which we have observed in the three-dimensional (3D) contour surfaces of the electron density we consider the root-mean-square deviation from uniform electron density. If our system consisted of N atomic cores of radius a into which the electron density could not penetrate, the free volume available to the electron density would be $V_F = L^3 - (4/3)\pi a^3 N$, where L is the side length of our simulation cell. If the electron density were spread uniformly throughout this free region, its value at all points outside the cores would be $\rho^F = 1/V_F$. We define our normalized root-mean-square deviation from uniform density as

$$\chi = \frac{1}{\rho^F}\left[\sum_i (\rho_i^T - \rho^F)^2\right]^{1/2}, \tag{4.1}$$

where the sum extends over all points on our grid which are not in the regions of the cores and ρ_i^T are the values of the electron density at these grid points. We use a value of $a=0.29\sigma$ for the core radius in our calculations on xenon,[6] though the results are insensitive for any reasonable choice of this parameter. Smaller values of χ are indicative of states with more uniform electron density, while more localized states are characterized by larger χ values.

Figure 11 shows the density dependence of χ in xenon for various system sizes. The general trend we see is that at

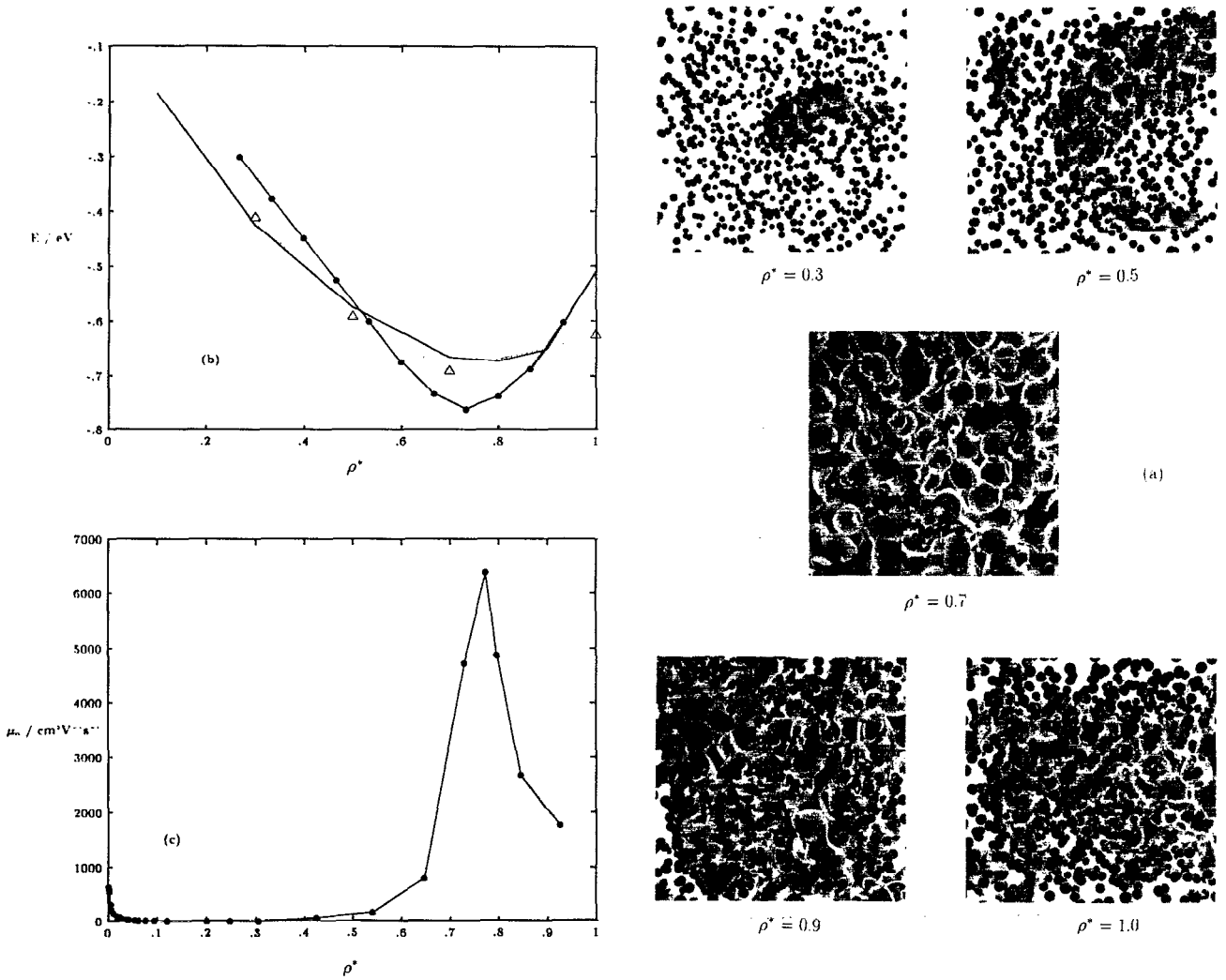

FIG. 10. (a) Same as Fig. 6(b) except configurations of the electron–unperturbed fluid xenon system are displayed here. (b) Experimental V_0 values (solid circles) and calculated ground-state energy values in xenon (density-dependent mean-field polarization potential, solid curve). Full many-body polarization results are presented as the triangles with the dotted curve. (c) Experimental zero-field mobility results (Refs. 46 and 47).

low solvent density χ is large, it goes through a minimum at the density where the experimental V_0 and μ_0 results have their extreme values, then it increases again at higher solvent densities. This behavior becomes more pronounced as the system size is increased. These trends in χ are completely consistent with our qualitative understanding of the 3D contour surfaces of the electron density discussed above. At low solvent densities the ground-state electron density is more localized, giving large values of χ associated with the considerable deviations from uniform electron density. Around the density where V_0, E_0, and μ_0 are extreme, the ground-state electron density is more uniformly spread throughout our fluid sample and χ reaches its minimum value. At higher densities χ increases again corresponding to the departure from uniform electron density associated with the breaking up of the electron density due to the growing importance of the electron interactions with the solvent atom cores.

Space and Coker[32] show that if the electron is localized at a particular solvent density, the rms deviation measure

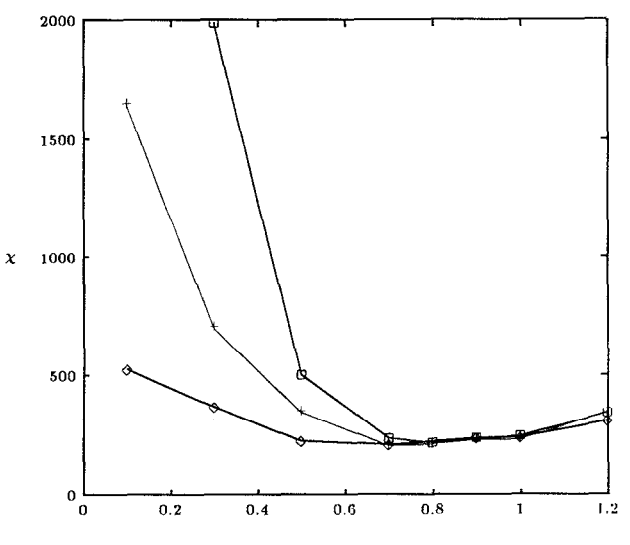

FIG. 11. Density dependence of the root-mean-square deviation from uniform electron density in fluid xenon. Diamonds denote the $N=256$ particle system, pluses denote $N=864$, and squares denote $N=2048$.

should increase like $N^{1/2}$ as the number of particles in the system N becomes large. If the electron is delocalized, on the other hand, the rms deviation from uniformity will be independent of the number of particles in the system.

We see that at low solvent densities the values of χ are very strongly system size dependent. As the density is increased, however, the values of χ for different system sizes all converge around the density where V_0 and μ_0 have their extreme values. Above this density the χ values are remarkably insensitive to system size and increase steadily as we approach the solid. This system size dependence results because at low densities the electron becomes localized on density fluctuations in the fluid. The density fluctuations on which the electron localizes may be comparable in size to the actual system when small systems are considered. As such, the importance of the regions devoid of electron density will be underestimated for these small systems and our rms deviation measure of localization will give small values as it is unable to sense the localization since the electron looks delocalized on the small system length scale. As the system size is increased, however, and the density fluctuations on which the electron localizes become a smaller fraction of the system volume, the rms deviation measure will see the regions devoid of electron density and thus sense the nonuniformity of the charge distribution. When we reach the threshold density where the rms deviation measure becomes independent of system size the ground-state electron density is even delocalized over the largest system sizes we consider. Space and Coker have studied larger systems ($\sim 10^4$ particles) and these findings persist.

In Figs. 10(b) and 10(c) we present our calculated ground-state energies and the experimental V_0 results as functions of density, together with experimental results for the density dependence of the electron mobility in xenon.[46,47] We see that there is a strong correlation between the density at which the mobility has its pronounced maximum and the minimum in V_0. This is also the same density at which our calculated ground-state electron density becomes uniformly spread throughout our fluid sample. It seems that when the ground state becomes uniformly spread throughout our fluid sample the electron mobility is high. When the wave function becomes spatially fragmented as we see at low and, to a lesser extent, at high densities the electron mobility is low. Our rms deviation from uniform electron density is an order parameter which seems to qualitatively track with the density dependence of the mobility. Similar types of ideas have been discussed by Coker, Thirumalai, and Berne[3] and have been formalized recently in the lakes-to-oceans percolation model developed by Stratt and co-workers.[22]

To test the accuracy of the density-dependent, mean-field, pair potential description of the many-body polarization interactions we have used the full solution of the system of self-consistent dipolar field equations in Eq. (3.2) to compute the many-body interaction potential which we use in our ground-state energy calculations. These ground-state energy results are compared with the mean-field results in Fig. 10(b). We see that across the whole range of densities the agreement between the mean-field and full self-consistent many-body results is quite good. At higher solvent densities the full self-consistent many-body results lie about 8%–10% below the mean-field values while at lower solvent densities they are in excellent agreement.

Even with the use of an accurate repulsive local pseudopotential and full self-consistent many-body treatment of dipole polarizability interactions we see from Fig. 10(b) that over the intermediate density regime where V_0 has its minimum our calculated ground-state energies are inconsistent with experimental V_0 values since they lie above these results and should provide a rigorous lower bound. The two most likely causes for this inconsistency are as follows:

(1) Approximating the nonlocal exchange and orthogonality terms appearing in the repulsive part of the pseudopotential with a fitted local form. This local approximation may not have the flexibility to describe the short-range nonlocal repulsive interactions.

(2) In our treatment of the many-body polarization we ignore interactions between induced higher-order multipole moments, truncating at induced dipolar terms. With a species as strongly polarizable as xenon it is likely that induced quadrupolar interactions and higher induced moments could be appreciable.

In gauging the magnitude of the two effects it should be noted that the neglect of the higher-order polarizabilities is to some extent compensated by the fact that the phase shifts are fit using this assumption. Nonlocal effects are simply assumed to be absent, i.e., $l=0$ effects are dominant. In addition, we have assumed that the repulsive part of the pseudopotential remains unchanged from the gas phase (even a nonlocal potential would be fit to gas-phase data). Perhaps for highly polarizable atoms the transferability assumption breaks down slightly.

C. Argon

Our ground-state energy results for the electron–argon system are presented in Fig. 12(b). Again, we see that when many-body polarization effects are ignored the calculated ground-state energy values do not show a minimum as a function of density until extremely high, unphysical solvent densities. When many-body polarization effects are included using the mean-field pair potential we see that the calculated ground-state energies show a minimum at the appropriate density. Also, in contrast to the behavior found in xenon, the ground-state energies in argon are brought into excellent agreement with experiment.[2] We have checked the calculated ground-state energy obtained with the mean-field pair potential against the results obtained with the full many-body treatment at $\rho^*=0.5$ and find that the agreement is quite good.

The almost quantitative agreement between the experimental conduction-band energies and our calculated ground-state energies is distinct from xenon where we observed some differences. This can be attributed to two factors: Since argon is both smaller and less polarizable than xenon, the effect of both nonlocal corrections and higher-order polarizabilities is diminished. In addition, the V_0

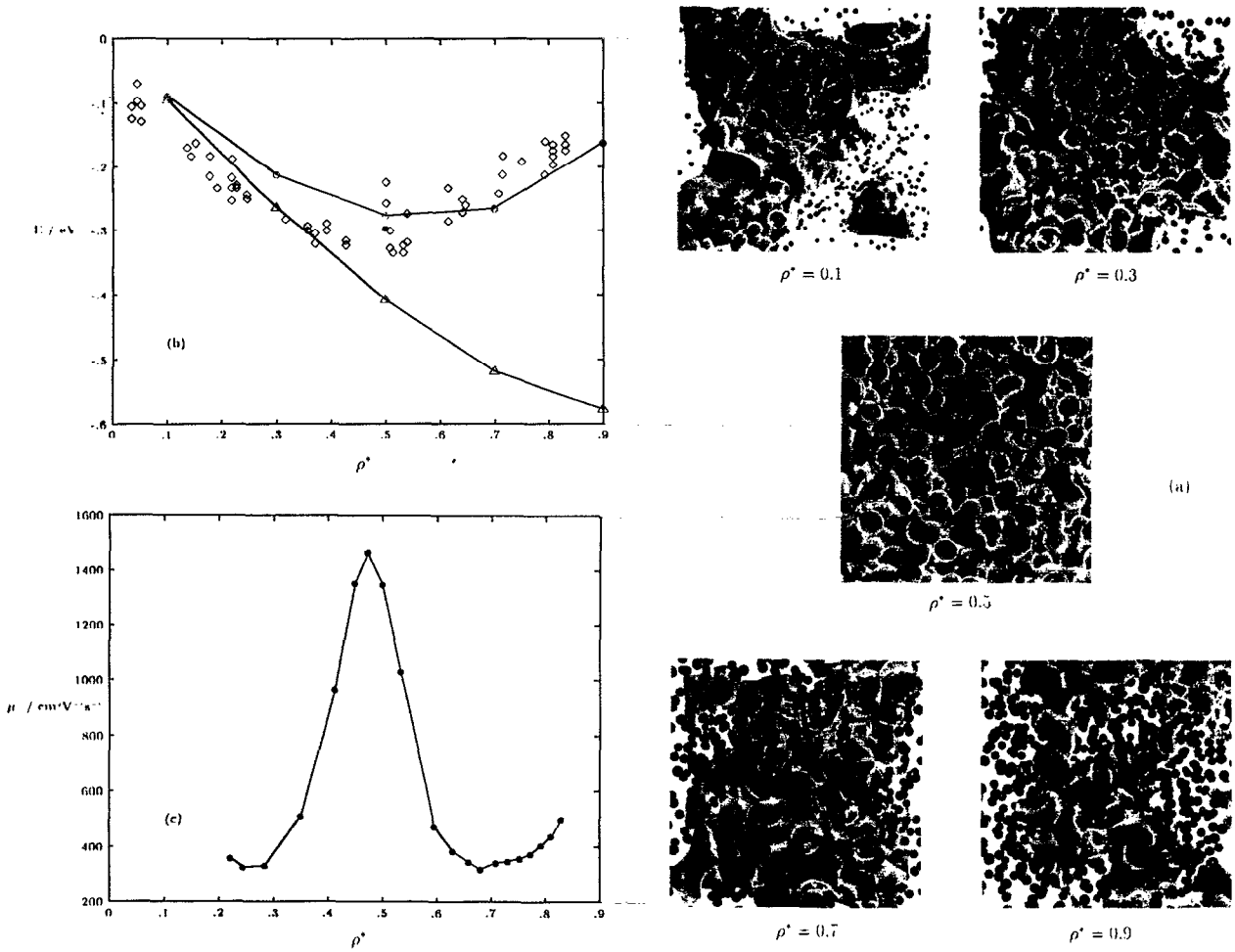

FIG. 12. (a) Same as Fig. 6(b) except configurations of the electron–unperturbed fluid argon system are displayed here. (b) Experimental V_0 values (diamonds) and calculated ground-state energy values in argon (density-dependent mean-field polarization potential, open circles). Triangles denote the ground-state energy computed using the bare pair potential. Solid circles denote the ground-state energy for a full many-body polarization calculation. (c) Experimental zero-field mobility results (Ref. 48).

curve in xenon showed a sharper density dependence than that of argon. Only around the minimum in V_0 do we see oceanlike states in xenon. The results described above for argon suggest that as V_0 must be an upper bound to the ground-state energy, the ground state in argon is percolative or close to percolative across a large range of fluid densities.

The 50% isosurfaces of electronic density in various representative fluid configurations at different densities in argon are presented in Fig. 12(a). We see that in argon the 50% isosurfaces are always fairly delocalized across our fluid sample over the entire range of fluid densities in agreement with the above conjectures. The general density dependence of the isosurfaces is similar to that observed in xenon. At low densities there are sizable regions devoid of electron density, at intermediate density ($\rho^*=0.5$ for argon) the electron density becomes uniformly spread throughout our fluid sample, and at high solvent density we see that the electron density becomes fragmented as channels are closed off by the repulsive solvent cores. Remarkably, just as we observed in xenon, the most delocalized electronic wave functions occur at the minimum in V_0 and the mobility maximum $\rho^* \sim 0.5$ [see Figs. 12(b) and 12(c)]. We again emphasize that the main difference between the isosurfaces in argon and those presented in Fig. 10(a) for xenon is that the states in argon are much more delocalized at low solvent density. Away from the region of the minimum in V_0 or maximum mobility the isosurfaces have more holes in them but they still extend over the entire system in contrast to the situation in low-density xenon.

The differences in the density dependence of the electronic ground state between argon and xenon discussed above are underscored by the experimental mobility values[46–48] which we reproduce in Fig. 13. Here we see that the mobility in xenon, despite its very large value at intermediate fluid densities, is very small below solvent densities of $\rho^* \sim 0.3$. In argon, on the other hand, we see that the mobility is quite sizable across the entire range of solvent densities consistent with the notion of a percolative ground state persisting throughout the fluid density regime.

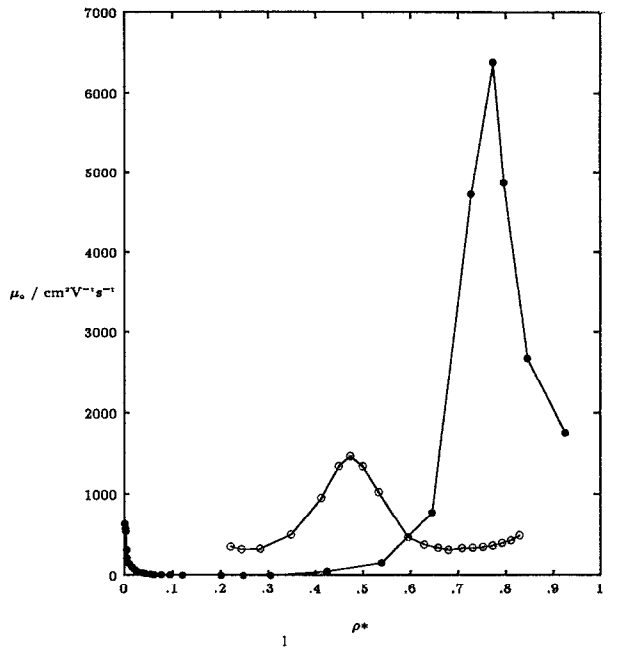

FIG. 13. Experimental zero-field electron mobility results in liquid argon (open circles) and xenon (solid circles).

V. CONCLUSION

The central theme of this paper has been the importance of many-body polarization interactions for the accurate description of excess electrons in fluids of highly polarizable molecules. The most dramatic evidence for the considerable significance of these interactions in determining excess electronic properties in these types of systems was presented in Fig. 8(b), where we showed our calculated ground-state energies in xenon across a very broad range of densities extending from the low-density fluid out to the very-high-density solid. We see that when the many-body induced-dipole polarization interactions are included through the use of the density-dependent mean-field pair potential the ground-state energies show a sharp minimum in the dense fluid and rise very steeply as solid densities are approached. This behavior is in very good qualitative agreement with the density dependence of the experimental conduction-band energies. When the many-body polarization interaction is ignored and the bare pair potential is used the calculated ground-state energies continue to decrease with increasing solvent density throughout the liquid and well into the highly compressed solid regime of densities. We see that, depending on the pseudopotential employed, the ground-state energy obtained with the bare pseudopotential may turn up at highly unphysical solvent densities at least 2–3 times that observed experimentally.

The ground-state energies obtained with the bare pair potential do not show even the vague qualitative trends with density that are observed in the experimental V_0 values or in the ground-state energies calculated with many-body polarization. It therefore seems unlikely that any theory of electrons in condensed polarizable media which ignores the many-body nature of interactions can provide physically reliable results. This brings into question the recent work of Stratt and co-workers in which they use a semiclassical percolation approach to estimate conduction-band energies in rare-gas fluids. The key feature of the theory developed by these authors is a pair potential component which represents the local kinetic energy of the electron in the fluid. They obtain a form for this kinetic pair potential by using a Jastrow form for the electronic wave function which is a pair product of hard-sphere scattering wave functions. This approximation should be quite good as the variational functions used in our diffusion Monte Carlo calculations were of this form and gave a very good description of the states. However, the results of the theory are very sensitive to the choice of the distance of closest approach between the electron and the hard-sphere scatterer. For this distance of closest approach in their Jastrow factor, Stratt and co-workers take the zero of the electron solvent pseudopotential. In this work they use the bare pair potential due to Siska which gives this distance of closest approach parameter as 1.786 Å in xenon. Stratt makes no attempt to optimize this choice of parameter value. Interestingly, we have calculated the ground-state energy for the pair Siska potential and the Siska potential with the many-body polarization term and have found that again with the pair potential E_0 is monotonically decreasing over the whole fluid range of densities, whereas for the many-body case, E_0 has a minimum at around $\rho^*=0.7$, but this value is much higher than either the experimental V_0 result or the E_0 values obtained with the Thirumalai or fitted potentials including many-body polarization.

Laria and Chandler parametrized their RISM-polaron theory for electrons in xenon in terms of an identical distance of closest approach parameter. This parameter enters the two theories in different ways but its interpretation is the same. Laria and Chandler found a consistent way to fit their distance of closest approach so that the theory gave results in reasonable agreement with simulation results of Coker, Thirumalai, and Berne[3] in both helium and xenon. These early simulation calculations used the bare pair polarization potential of Thirumalai. The value Laria and Chandler found for the closest approach distance for the electron in xenon was 1.176 Å, i.e., about 30% smaller than the value Stratt uses in his theory. In Fig. 6 of their paper, Stratt and co-workers report that reducing the distance of closest approach value by as little as only 5% from their 1.786 Å value causes the minimum of their calculated V_0 values to drop from -0.68 eV to -0.9 eV and the position of this minimum shifts out in density from $\rho^*=0.8$ to $\rho^*=0.867$. A reduction of 30% in the distance of closest approach to be consistent with the Laria–Chandler value would probably shift the minimum in the calculated V_0 curve considerably further out in density and down in energy, and considering the neglect of many-body polarization in these theoretical results these sorts of shifts may bring their calculated conduction-band energies into consistency with the ground-state energy results we present in Fig. 8(b) when the many-body polarization interactions are ignored.

We are thus left to surmise that the agreement between

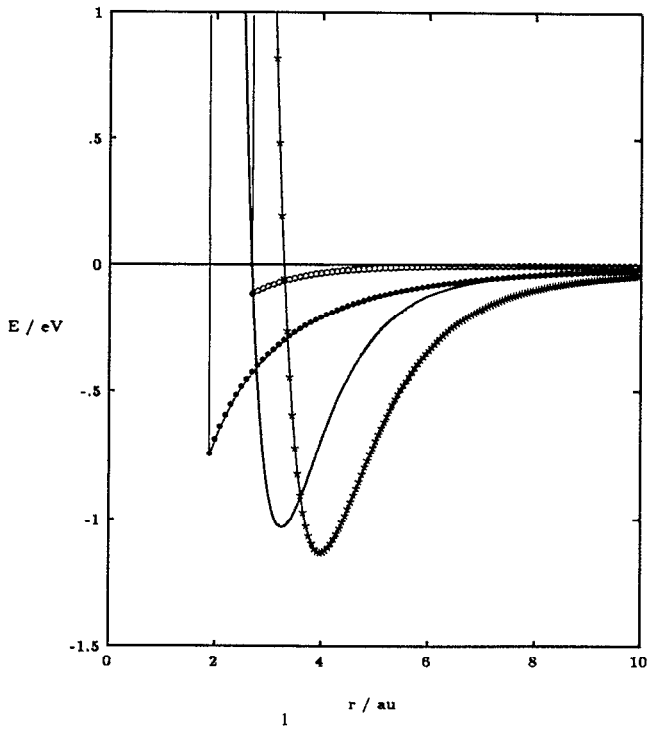

FIG. 14. Comparison of Hsu and Chandler's fitted Yukawa excess electron pseudopotentials for argon (solid circles) and xenon (open circles) with our fitted potentials for argon (solid curve) and xenon (stars).

experiment and Stratt's theoretical results for the density dependence arises fortuitously. The curvature in V_0 probably arises from an overestimation of the kinetic energy rather than from a leveling off of the average potential energy. It would be very interesting to see how Stratt's lakes-to-oceans percolation theory performed using a realistic parametrization together with the density-dependent mean-field potentials to treat the many-body nature of the induced polarization interaction.

Recently, Hsu and Chandler[21] analytically continued the RISM polaron theory and calculated the mobility of excess electrons in argon and xenon. They used a hard-sphere model for the solvent–solvent interactions and a hard sphere with an attractive Yukawa tail beyond the distance of closest approach. They found that by adjusting the potential parameters, i.e., controlling the relative importance of the attractive and repulsive components of the electron–solvent pseudopotential they could obtain a maximum in the electron mobility as a function of solvent density. They were able to obtain a reasonable fit to the peak position with a single density-independent pair electron–solvent pseudopotential which included no explicit many-body treatment of the induced polarization interaction.

In Fig. 14 we compare the Yukawa forms which Hsu and Chandler obtained by fitting to the mobility data in both argon and xenon with pseudopotentials which we have used in our calculations. Because of the nonuniqueness of the pseudopotential description of the electron–solvent interactions we cannot easily compare pseudopotentials for different systems unless they are best fits with the same functional form. Our best-fit pseudopotentials which reproduce available gas-phase scattering data are the fitted potentials which, as discussed in Sec. III, have the same form for the repulsive core and long-range attraction in both argon and xenon, but the polarization switching functions are different. The general trend observed for our accurate pseudopotentials as we increase the polarizability of the target atom (going from argon to xenon) is that the core gets larger and the attraction gets stronger, resulting in a deeper well. If identical attractive potential forms were used (i.e., if we used the same switching function form in argon and xenon) this trend of deeper wells with larger polarizability would be even more pronounced as evidenced by the potentials presented by Siska (see Fig. 2 of Ref. 49). The physical reasons for these trends are clear: The heavier xenon atom has a larger core than argon and the resulting larger polarizability of xenon can lead to larger attractive interactions.

From Fig. 14 we see that the forms obtained by Hsu and Chandler by fitting their theoretical results to experimental mobility data do not show the trends expected when a fixed form of pseudopotential is used to represent electron–atom interactions in argon and xenon. We see that the core size they find does show the correct trend; increasing as we go from argon to xenon, but the attractive components of the interactions obtained from Hsu and Chandler's fit of their theory to experiment are completely unphysical. They find that the attractions in the more polarizable xenon system are much smaller than in argon, resulting in the highly implausible finding that the pseudopotential well depth in xenon is between 6 and 7 times shallower than that in argon. Apparently, the experimental mobility data in xenon can also be fit with a more physically reasonable parametrization of the Yukawa tail pseudopotential which is deeper than that for argon.[50]

Hsu and Chandler also calculated the mean electronic energy as a function of solvent density using their fitted models in both argon and xenon and found that this thermally averaged energy decreased with increasing solvent density across the entire range of liquid densities they considered. Admittedly, the mean electronic energy is not the conduction-band energy which experimentally shows a minimum and upturn as a function of increasing solvent density over this range but as the density dependence of the excited-state energies track that of the ground-state energies[32] the canonically averaged energy should show similar trends. In early path-integral studies of the mean energy of excess electrons in xenon, Coker and Berne[17] explicitly treated the many-body polarization interactions and found evidence for a slight upturn in the thermally averaged electronic energy. Recently, similar calculations have been repeated in argon by Lopez-Castillo *et al.*,[18] who used a similar mean-field many-body polarization potential together with large system sizes, many more path-integral beads, and very long runs. The results of their detailed studies indicate that the mean excess electronic energy in argon goes through a minimum and follows the density dependence of the experimental V_0 values very closely. The fact that Hsu and Chandler's density-independent potentials,

which are fit to give the experimental mobilities, fail to reproduce any other experimental property is consistent with the inadequacy of a density-independent pair potential description of the interactions in these highly polarizable fluids.

Nichols and Chandler[51] used RISM-polaron theory to study an electron in a fluid composed of hard spheres with embedded Drude oscillators to model an electron in a polarizable fluid. This model should include most of the effects which we have found to be important in determining properties such as the density dependence of the ground-state energy. With this model it would be unnecessary to fit the theory to experiment as Hsu and Chandler have had to do with their pair potential form. In principle, one could simply repeat our approach and fit the short-range parts of the potential (the hard-sphere radius and polarization switching function in their model) and fix the parameters of the Drude oscillator part of the potential assuming a high-frequency polarization response using the correct polarizability to give the gas-phase scattering results. We believe that parametrizing the approach of Nichols and Chandler in this way would not only give equilibrium results in good agreement with experiment but also possibly resonable dynamical properties. Nichols and Chandler used a parametrization of their potential which was not close to values expected for realistic systems and as such they did not see mobility maxima but did find an upturn in the excess electron energy as a function of density.

A number of workers have discussed the anomolous density dependence of the electron mobility in the heavier rare gases in terms of a condensed-phase analog of the Ramsauer–Townsend effect of gas-phase electron–atom scattering.[21,46,47] The idea behind the gas-phase phenomenon is that the scattering amplitude depends on the phase shift of the scattering wave function at large distances, relative to the free-particle wave function. If the potential has a strong enough attraction it can drag the oscillations of the wave function in towards the scattering center to such an extent that the scattered wave function appears to be unshifted from that of the free particle and the scattering amplitude vanishes giving no scattering as though the scattering center was transparent. The idea behind the condensed-phase analog, on the other hand, is that if we consider integrating the potential or "force" experienced by the electron over the region occupied by the electron and weighting by the electron density, when the solvent atoms are positioned appropriately relative to one another and the electron, there will be a cancellation between the integrated attractive and repulsive forces giving no net force on the electron as a whole so under these conditions the fluid becomes transparent to the electron and a high mobility results. Under other conditions the electron–solvent system may be arranged in such a way that either attractive or repulsive forces dominate when we integrate over the wave function, thus giving lower mobilities.

We suggest that our channel or percolation model is entirely consistent with this Ramsauer–Townsend interpretation. At low solvent densities our channel model clusters give regions of the fluid which, when integrated over the electron density, are more attractive than the surrounding lower-density regions. At intermediate solvent densities the atoms are positioned in such a way to give overlapping potential wells forming a connected arrangement of channels. Under these conditions all regions of the fluid offer a similar average potential when integrated over the spatial extent of the electron. There is thus no preference for the electron to localize in any one region in the fluid compared to any other region. At higher solvent densities the repulsive wall of the electron–solvent interaction becomes more important, associated with our channels becoming closed off. In the condensed-phase Ramsauer–Townsend interpretation this corresponds to there being a net repulsive interaction upon integrating over the volume occupied by the electron.

ACKNOWLEDGMENTS

D. F. C. and B. S. gratefully acknowledge financial support for this work from the National Science Foundation (Grant No. CHE-8913780 and Grant No. CHE-9058348), and from the Petroleum Research Fund administered by the American Chemical Society (Grant No. 22238-AC6), and a generous allocation of supercomputer time from the National Center for Supercomputing Applications. These authors also thank Glenn Bresnahan for computer graphics support, and David Hsu for useful discussions of RISM polaron theory results. B. J. B. and Z. H. L. gratefully acknowledge financial support for this work from the National Science Foundation (Grant No. CHE-87-00522) and from the National Institutes of Health (Grant No. 1 RO1 GM43340-01A1). G. M. would like to acknowledge an NSF Postdoctoral Research Associateship in Computational Science and Engineering (No. ASC-91-08812).

APPENDIX: EXPECTATION VALUES IN DIFFUSION MONTE CARLO

In the Appendix, we derive Eq. (2.2). Define $u(\mathbf{r}) = \psi_0(\mathbf{r}) - \psi_T(\mathbf{r})$ where $\psi_0(\mathbf{r})$ is the normalized ground-state wave function and $\psi_T(\mathbf{r})$ is the normalized trial wave function. For any observable $\hat{A}$,

$$\int u(\mathbf{r})\hat{A}u(\mathbf{r})d^3\mathbf{r} = \int \psi_0(\mathbf{r})\hat{A}\psi_0(\mathbf{r})d^3\mathbf{r} - 2\int \psi_0(\mathbf{r})\hat{A}\psi_T(\mathbf{r})d^3\mathbf{r} + \int \psi_T(\mathbf{r})\hat{A}\psi_T(\mathbf{r})d^3\mathbf{r}. \quad \text{(A1)}$$

The first term on the right-hand side of the above equation is the expectation value of $\hat{A}$ in the ground state and the third term is the expectation value in the trial state which is given. Since we are sampling the importance function $f_0 = \psi_0\psi_T$ in DMC, it is useful to rewrite the expectation value given in Eq. (A1) in terms of $f_0(\mathbf{r})$. The second term in Eq. (A1) can be expressed as

$$\int \psi_0(\mathbf{r})\hat{A}\psi_T(\mathbf{r})d^3\mathbf{r} = \int f_0(\mathbf{r})\frac{\hat{A}\psi_T(\mathbf{r})}{\psi_T(\mathbf{r})}d^3\mathbf{r}. \quad \text{(A2)}$$

$f_0(\mathbf{r})$ is an unnormalized distribution function and we define averages over it as

$$\langle[\cdots]\rangle_{f_0} \equiv \frac{\int f_0(\mathbf{r})[\cdots]d^3\mathbf{r}}{\int f_0(\mathbf{r})d^3\mathbf{r}}. \quad \text{(A3)}$$

These averages are evaluated by direct sampling in DMC. This allows us to write the right-hand side of Eq. (A2) in terms of $\langle[\cdots]\rangle_{f_0}$ as

$$\int \psi_0(\mathbf{r})\hat{A}\psi_T(\mathbf{r})d^3\mathbf{r} = \left\langle\frac{\hat{A}\psi_T}{\psi_T}\right\rangle_{f_0}\int f_0(\mathbf{r})d^3\mathbf{r}. \quad \text{(A4)}$$

Now since $u^2 = \psi_0^2 + \psi_T^2 - 2f_0$, it follows that

$$\int f_0(\mathbf{r})d^3\mathbf{r} = 1 - \frac{1}{2}\int u^2(\mathbf{r})d^3\mathbf{r}. \quad \text{(A5)}$$

Substitution of Eqs. (A4) and (A5) into the second term of Eq. (A1), expressing $\int\psi_T(\mathbf{r})\hat{A}\psi_T(\mathbf{r})d^3\mathbf{r}$ as $\langle\hat{A}\psi_T(\mathbf{r})/\psi_T(\mathbf{r})\rangle_{\psi_T^2(\mathbf{r})}$ and followed by rearrangement gives

$$\int \psi_0(\mathbf{r})\hat{A}\psi_0(\mathbf{r})d^3\mathbf{r}$$
$$= 2\left\langle\frac{\hat{A}\psi_T(\mathbf{r})}{\psi_T(\mathbf{r})}\right\rangle_{f_0(\mathbf{r})} - \left\langle\frac{\hat{A}\psi_T(\mathbf{r})}{\psi_T(\mathbf{r})}\right\rangle_{\psi_T^2(\mathbf{r})}$$
$$+ \int u(\mathbf{r})\left[\hat{A} - \left\langle\frac{\hat{A}\psi_T(\mathbf{r})}{\psi_T(\mathbf{r})}\right\rangle_{f_0(\mathbf{r})}\right]u(\mathbf{r})d^3\mathbf{r}. \quad \text{(A6)}$$

[1] R. Reininger, U. Asaf, and I. T. Steinberger, Chem. Phys. Lett. **90**, 287 (1982).
[2] R. Reininger, U. Asaf, I. T. Steinberger, and S. Basak, Phys. Rev. B **28**, 4426 (1983).
[3] D. F. Coker, D. Thirumalai, and B. J. Berne, J. Chem. Phys. **86**, 5689 (1987).
[4] M. Sprik, M. L. Klein, and D. Chandler, Phys. Rev. B **31**, 4234 (1985).
[5] M. Sprik, M. L. Klein, and D. Chandler, J. Chem. Phys. **83**, 3042 (1985).
[6] D. Laria and D. Chandler, J. Chem. Phys. **87**, 4088 (1987).
[7] D. F. Coker and B. J. Berne, J. Chem. Phys. **89**, 2128 (1988).
[8] B. E. Springett, M. H. Cohen, and J. Jortner, Phys. Rev. **159**, 183 (1967).
[9] B. Plenkiewicz, P. Plenkiewicz, and J. P. Jay-Gerin, Phys. Rev. A **40**, 4113 (1989).
[10] B. Plenkiewicz, P. Plenkiewicz, and J. P. Jay-Gerin, Chem. Phys. Lett. **163**, 542 (1989).
[11] B. Plenkiewicz, J. P. Jay-Gerin, P. Plenkiewicz, and G. B. Bachelet, Europhys. Lett. **1**, 455 (1986).
[12] P. Stampfli and K. H. Bennemann, Phys. Rev. A (to be published).
[13] A. Wallqvist, G. Martyna, and B. J. Berne, J. Phys. Chem. **92**, 1721 (1988).
[14] G. Martyna and B. J. Berne, J. Chem. Phys. **89**, 4516 (1988).
[15] G. J. Martyna and B. J. Berne, J. Chem. Phys. **90**, 3744 (1989).
[16] J. Lekner, Phys. Rev. **158**, 130 (1967).
[17] D. F. Coker and B. J. Berne, in *Excess Electrons in Dielectric Media*, edited by C. Ferradini and J. P. Jay-Gerin (CRC, Boca Raton, FL 1991), pp. 211–257.
[18] J. M. Lopez-Castillo, Y. Frongillo, B. Plenkiewicz, and J. P. Jay-Gerin, J. Chem. Phys. (submitted).
[19] P. Stampfli and K. Bennemann, Phys. Rev. A **71**, 1674 (1988).
[20] D. Thirumalai, in *Large Finite Systems*, edited by J. Jortner (Reidel, New York, 1987).
[21] D. Hsu and D. Chandler, J. Chem. Phys. **93**, 5075 (1990).
[22] S. H. Simon, V. Dobrosavljevic, and R. M. Stratt, J. Chem. Phys. **94**, 7360 (1991).
[23] F. Webster, P. J. Rossky, and R. A. Friesner, Comput. Phys. Commun. **63**, 494 (1991).
[24] J. K. Cullum and R. A. Willoughby, *Lanczos Algorithms for Large Symmetric Eigenvalue Computations* (Birkhauser, Boston, 1985).
[25] R. Kosloff, J. Phys. Chem. **92**, 2087 (1988).
[26] J. B. Anderson, J. Chem. Phys. **63**, 1499 (1975).
[27] J. B. Anderson, J. Chem. Phys. **65**, 4121 (1976).
[28] J. B. Anderson, J. Chem. Phys. **82**, 2662 (1984).
[29] J. B. Anderson, J. Chem. Phys. **73**, 3897 (1980).
[30] D. M. Ceperley and M. H. Kalos, in *Monte Carlo Methods in Statistical Physical Physics*, edited by K. Binder (Springer, Berlin, 1979), p. 145.
[31] D. M. Ceperley and B. Bernu, J. Chem. Phys. **89**, 6316 (1988).
[32] B. Space and D. F. Coker (in preparation).
[33] B. Space and D. F. Coker, J. Chem. Phys. **94**, 1976 (1990).
[34] B. Space and D. F. Coker, J. Chem. Phys. **96**, 652 (1992).
[35] R. P. McEacharan and A. D. Stauffer, J. Phys. B **16**, 255 (1983).
[36] J. F. Williams, J. Phys. B **12**, 265 (1979).
[37] M. V. Rama Krishna and K. B. Whaley, Phys. Rev. B **38**, 11 839 (1988).
[38] R. K. Nesbet, Phys. Rev. A **20**, 58 (1979).
[39] N. R. Kestner, J. Jortner, M. H. Cohen, and S. A. Rice, Phys. Rev. **140**, A56 (1965).
[40] D. Thirumalai (unpublished).
[41] U. Asaf and I. T. Steinberger, Chem. Phys. Lett. **128**, 91 (1986).
[42] W. T. Sommer, Phys. Rev. Lett. **12**, 271 (1964).
[43] M. A. Woolf and G. W. Rayfield, Phys. Rev. Lett. **15**, 235 (1965).
[44] J. A. Northby and T. M. Sanders, Phys. Rev. Lett. **18**, 1184 (1967).
[45] J. R. Broomall, W. D. Johnson, and D. G. Onn, Phys. Rev. B **14**, 2819 (1976).
[46] S. S. S. Huang and G. R. Freeman, J. Chem. Phys. **68**, 1355 (1978).
[47] S. S. S. Huang and G. R. Freeman, Phys. Rev. A **24**, 714 (1981).
[48] J. A. Jahnke, L. Meyer, and S. A. Rice, Phys. Rev. A **3**, 734 (1971).
[49] P. E. Siska, J. Chem. Phys. **71**, 3942 (1979).
[50] D. Hsu (private communication).
[51] A. L. Nichols III and D. Chandler, J. Chem. Phys. **84**, 398 (1986).
[52] S. Basak and M. H. Cohen, Phys. Rev. B **20**, 3404 (1979).
[53] R. P. McEacharan and A. D. Stauffer, J. Phys. B **16**, 4023 (1983).
[54] R. P. McEacharan and A. D. Stauffer, J. Phys. B **17**, 2507 (1984).